applied sciences

MDPI

Review

Molecular Imaging with ^{68}Ga Radio-Nanomaterials: Shedding Light on Nanoparticles

Irene Fernández-Barahona [1], María Muñoz-Hernando [1], Juan Pellico [1,2], Jesús Ruiz-Cabello [2,3,4,5] and Fernando Herranz [1,2,*]

1 Centro Nacional de Investigaciones Cardiovasculares Carlos III (CNIC), C/Melchor Fernández-Almagro 3, 28029 Madrid, Spain; irene.fernandezbarahona@cnic.es (I.F.-B.); maria.munoz@cnic.es (M.M.-H.); juan.pellico@cnic.es (J.P.)
2 Centro de Investigación Biomédica en Red (CIBERES), 28029 Madrid, Spain; jruizcabello@cicbiomagune.es
3 CIC biomaGUNE, Paseo de Miramón 182, 20014 Donostia-San Sebastián, Spain
4 Ikerbasque, Basque Foundation for Science, 48013 Bilbao, Spain
5 Departamento Química Física II, Facultad de Farmacia, Universidad Complutense de Madrid, 28040 Madrid, Spain
* Correspondence: fherranz@cnic.es

Received: 17 May 2018; Accepted: 29 June 2018; Published: 6 July 2018

Abstract: The combination of radioisotopes and nanomaterials is creating a new library of tracers for molecular imaging, exploiting the sensitivity of nuclear imaging techniques and the size-dependent properties of nanomaterials. This new approach is expanding the range of applications, including the possibility of theranostics. Among the many different combinations, the use of ^{68}Ga as the radioisotope in the radio-nanomaterial is particularly convenient. The physicochemical properties of this isotope allow incorporating it into many materials with great chemical flexibility. Furthermore, its production from a benchtop generator eases the preparation of the tracer. Here, we review main results from the last years in which a nanomaterial has been radiolabeled with ^{68}Ga. In thus process, we pay attention to the use of nanomaterials for biomedical imaging in general and main properties of this radioisotope. We study the main methods to carry out such radiolabeling and the most important applications for molecular imaging.

Keywords: Gallium-68; radio-nanomaterials; molecular imaging; biomedical imaging; nanoparticles; radiochemistry; nanomedicine

1. Introduction

Radiolabeled nanomaterials have emerged in the last years as a very promising tool for molecular imaging applications [1]. The combination of the size-dependent properties of nanomaterials with the sensitivity of radioisotopes in nuclear imaging techniques opens an attractive field in the development of new probes for the diagnosis and treatment of different pathologies. In terms of molecular imaging, the combined use of a radioisotope and a nanoparticle (NP) completely change the role of the latter. The possibility of using nanoparticles for in vivo "hotspot" imaging increases the usefulness of nanomaterials in biomedical imaging. For example, one of the reasons iron oxide nanoparticles have not replaced Gd-based agents in clinical practice is the typical dark contrast these nanoparticles provide. This can be a problem for many pathologies, where endogenous hypointense areas in magnetic resonance imaging (MRI) are common. The combination of this kind of nanomaterial with a radioisotope eliminates this limitation. This is the rationale behind the title we have chosen for our revision; the addition of a radioisotope to most nanomaterials sheds light on their utility as tracers in molecular imaging.

Nanomaterials present an increased surface/volume ratio as one of their most exploited features. This particularity of materials at the nanometric scale, provides an enormous number of specific binding sites for multifunctionalization of nanomaterials with bioactive molecules for biomedical applications or other probes for multimodal imaging among multiple other possibilities. One of the reasons is the multiple combinations that emerge by just modifying three variables; type of nanomaterial, type of radioisotope and how the radioisotope is incorporated to the nanoparticle. Focusing on the last aspect, we can find surface radiolabeling, with or without a chelator, and core labeling. This last approach offers advantages concerning transmetallation and radioisotope detachment, at the cost of a more demanding synthesis, particularly time-wise when working with short half-life isotopes. In terms of type of nanomaterials and radioisotopes, almost all possible combinations have been achieved, although not all of them with the same practical usefulness from an imaging point of view. In the last years, it is easy to find examples with ^{18}F [2–4], ^{64}Cu [5–7], ^{69}Ge [8], ^{99m}Tc [9,10], $^{123/124/125/131}$I [11–16], or even ^{11}C [17]. The new role of nanomaterials in imaging, by virtue of this combination, is probably the most important advantage; however, it is not limited to that. Other aspects benefiting from this "marriage" are related, for example, with a precise and quantitative study of nanoparticle biodistribution, a relatively easy tuning of tracer pharmacokinetics or the possibility of using radioisotopes for therapeutic purposes.

The use of nanomaterials for nuclear imaging already has several important reviews summarizing the combination of different radioisotopes and nanoparticles [1,18–20]. However, there are none focusing in what is becoming a well-liked sector of ^{68}Ga-labeled nanoparticles. In this review, we see what the main features of this radioisotope are, making it probably the most relevant one at present in the field.

2. ^{68}Gallium

^{68}Gallium (^{68}Ga) is a positron emitter radioisotope with a half-life of 67.845 min that can be obtained from its parent radionuclide ^{68}Ge [21]. It decays to ^{68}Zinc with 89% positron branching and maximum energy of 1.9 MeV, and mean of 0.89 MeV [22]. Owing to its short half-life that matches the pharmacokinetics of small biomolecules, it is highly suitable for positron emission tomography (PET) imaging. It is one of the first short-lived β^+-emitting radionuclides to have been used in clinical imaging; long before the PET gold standard, ^{18}F-fluorodeoxyglucose (^{18}FDG), usage began. ^{68}Ga-ethylenediaminetetraacetic acid (^{68}Ga-EDTA) was used in the 1950s for brain tumor annihiscopy, a system based in coincidence detection used before PET appeared [23]. The most appealing advantage ^{68}Ga presents, and many other radionuclides used in PET do not, is it can be produced on site in a benchtop ^{68}Ge/^{68}Ga generator, avoiding the need for a cyclotron nearby.

2.1. ^{68}Ge/^{68}Ga Generators

Generators are devices used to produce useful short-lived daughter radionuclides from a long-lived radionuclide. These devices are often termed as "cows". Repeated separations of the daughter product are termed elutions and the process is colloquially referred to as "milking". A ^{68}Ge/^{68}Ga generator is used to extract ^{68}Ga from its parent isotope ^{68}Ge. ^{68}Ge decays by electron capture to ^{68}Ga that can then be eluted from the generator every few hours. As ^{68}Ge has a relatively long half-life ($T_{1/2}$ = 270.8 days), the use of the generator spans several months.

The first ^{68}Ge/^{68}Ga generator was described in 1960 using liquid–liquid extraction chemistry [24]. Several ^{68}Ga compounds, were synthesized with extraction product of this generator and used to scan intracranial lesions [25]. Later in the 1960s, the liquid–liquid extraction chemistry was substituted by a solid-phase-based ion exchange system. Trail-breaking studies used alumina (Al_2O_3) to retain ^{68}Ge, while ^{68}Ga could be eluted from the column using ethylenediaminetetraacetic acid (EDTA) [26,27]. Solid-phase chromatographic generators offered compelling radiochemical properties, being able to repeatedly elute in 95% yield and as little as 1.4×10^{-5}% of ^{68}Ge [28]. This system was economically convenient as a ^{68}Ga-EDTA source. However, eluate was troublesome for subsequent radiolabeling

processes because of the high thermodynamical stability of the ^{68}Ga-EDTA complex [29]. In the late 1970s, the impact of ^{68}Ga in nuclear imaging started to evanesce due to the inability of the available generators to meet the requirements of ^{68}Ga radiopharmaceutical syntheses. Furthermore, ^{99m}Tc- and ^{18}F-based imaging were rapidly developing and gaining clinical significance. This blend of difficulties motivated the quest for second-generation "ionic" generators.

Pioneer Russian radiochemists developed a new type of ^{68}Ge/^{68}Ga generator that became commercially available at the beginning of the 21st century [30]. Most common ^{68}Ge/^{68}Ga generators commercially available nowadays are based on hydrochloric acid and elute ^{68}Ga in cationic form ($^{68}Ga^{3+}$) rather than inert ^{68}Ga complexes [29,30]. "Fresh" generators elute yields 70–80%, decreasing over time. The rapid insertion of these generators to clinical environments raised concern on safety of eluate products for routine clinical use. ^{68}Ge breakthrough (ranging 0.01–0.001%), proton excess coming from hydrochloric acid used for elution and metallic impurities should be eliminated, as well as elution under current Good Manufacturing Practices (cGMP) conditions to ensure safe use. To achieve this, a "post-processing" or extra purification process is sought. This may be accomplished by: (i) fractionating eluate and selecting the fraction with the highest ^{68}Ga concentration; (ii) selectively trapping the anionic chloro-complexes of $^{68}Ga^{3+}$ using an anion-exchange resin; or (iii) using a cation exchange cartridge to selectively retain ^{68}Ga by elution using diluted HCl [30–32].

Current commercially available generators are inorganic oxide-based (SnO_2 or TiO_2) or use an organic resin [28]. Eckert and Ziegler (Berlin, Germany) commercialized clinically approved generators with a modified titanium oxide column eluted with 0.1 M HCl. Low specific volume of ^{68}Ga eluate is obtained and column packing material dissolution is a source of metal impurities. ^{68}Ga yield is greater than 60% of nominal activity and ^{68}Ge breakthrough is 0.0001% for fresh generators, slightly increasing as generator ages. Obninsk Cyclotron Ltd. (Obninsk, Russia) also commercialized these type of generators, however ^{68}Ge breakthrough is less than 0.005% and elution yield is higher than 75% for each elution. Generator is eluted with 0.1 M HCl and eluate volume is 5 mL.

Ithemba Labs (Cape Town, South Africa) produced SnO_2 column-based generators that can be eluted with 0.6–1 M HCl. Elution volume stands in 6 mL. They present low specific volume, high metallic ion impurities content in the eluate and require a stronger acidic solution for the elution in comparison to other generator systems. At calibration time, ^{68}Ga yield is higher than 80% and ^{68}Ge breakthrough less than 0.001% [33]. PARS Isotope Company (Tehran, Iran), commercializes a ^{68}Ga/^{68}Ge sterile generator named PARS-Gallugen®, with a SnO_2 column which is eluted with 1 M HCl with more than 99% radiochemical purity and radiochemical yield.

Silica gel-based (SiO_2, organic) generators were commercialized by ITG Isotope Technologies (Garching bei München, Germany). They are eluted with 0.05 M HCl and is GMP certified. Elution volume is 4 mL and elution yield is greater than 80%. ^{68}Ge breakthrough is expected to be less than 0.005% [33].

In 2015, IRE ELiT (Fleurus, Belgium) started commercializing Galli Eo®, ^{68}Ga/^{68}Ge generator eluted with 0.1 M HCl, with more than 67% yield and less than 0.001% ^{68}Ge breakthrough. Column matrix material is unspecified. It is produced under GMP conditions but is only intended for research and laboratory purposes in the European Union.

2.2. Small Molecule Clinical Applications of ^{68}Ga

Generator-based ^{68}Ga production offers a cost-effective alternative to cyclotrons and reactors. ^{68}Ga/^{68}Ge generators allow relatively inexpensive clinical PET studies in facilities where cyclotron-produced isotopes are hard to access or unavailable. Moreover, benchtop generators can be placed in the bench of a simple synthesis module; hence, space required is insignificant in comparison with a cyclotron. Accordingly, facile and rapid production of ^{68}Ga has highly promoted its use in molecular imaging [34]. Availability of commercial generator systems and efficient purification implementations have focused the attention of clinicians on ^{68}Ga. Favorable coordination chemistry that eases coupling to small biomolecules and gallium's affinity towards tumor tissue (it has been used as

chemotherapy agent) impulse ^{68}Ga as a potential alternative to ^{18}F- and ^{11}C-PET radiopharmaceuticals. Many ^{68}Ga complexes have been applied in nuclear medicine [22,35]. ^{68}Ga-EDTA was used to study blood–brain barrier integrity and renal function [36,37]. ^{68}Ga-citrate has been utilized to image infection in animal models and human patients [38,39]. ^{68}Ga-phosphonate complexes have served as bone metastases trackers in small animal models [40,41]. A derivative of tris(salicylaldimine), Tris(4,6-dimethoxysalicylaldimine)-N,N′-bis(3-aminopropyl)-N,N′-ethylenediamine (BAPEN), may be used as cardiac function radiotracer when radiolabeled with ^{68}Ga, forming ^{68}Ga-BAPEN [42,43]. ^{68}Ga-radiolabeled macroaggregated albumin (^{68}Ga-MAA) has been used for lung function and perfusion assessment [44–46].

As physical half-life of ^{68}Ga matches the biological half-life of numerous peptides and small molecules, the synergy of both seems a feasible approach to tackle the tracking of different biological phenomena. Somatostatin analog peptide use prevails in the literature. ^{68}Ga-DOTA-NOC, consisting of ^{68}Ga-DOTA (1,4,7,10-Tetraazacyclododecane-1,4,7,10-tetraacetic acid) complex conjugated to the somatostatin analog 1 (1-NaI3-octreotide, NOC) has been used for the detection of a broad range of tumor types and their metastases, as for example parotid basal cell adenoma, medulloblastoma, neuroblastoma and bronchial carcinoids [47–50]. Another complex using a different somatostatin analog (Tyr3-octreotate, TATE), ^{68}Ga-DOTA-TATE has also been used in several tumor-type detection and is part of ongoing clinical trials for metastatic castration-resistant prostate cancer diagnostics [51,52]. Edotreotide (TOC), with a special affinity for type 2 somatostatin receptors has also been used combined with ^{68}Ga-DOTA (^{68}Ga-DOTA-TOC) to diagnose cancerous lesions [53–55]. Bombesin, which is a peptide found in the intrinsic nerves of the gastrointestinal tract, has also been used in conjunction with ^{68}Ga to diagnose tumor lesions targeting gastrin-releasing peptide receptors [56,57]. Folate conjugates have also been employed to create targeted ^{68}Ga-based complexes for ovarian cancer detection [58].

^{68}Ga-Pentixafor, composed by a synthetic pentapeptide that targets the chemokine receptor type 4 (CXCR4) and DOTA chelating ^{68}Ga, has been used to diagnose prostate cancer in a PC-3 prostate cancer xenograft mouse model [59]. This radiotracer has also been used for the detection of CXCR4 in atherosclerotic plaques [60,61]; for neuroendocrine tumor detection; and is currently undergoing clinical trials in diagnosis of neuroendocrine tumors [62].

3. Radiolabeling Nanomaterials

Successful design and development of radiolabeled nanoprobes requires careful analysis and consideration of numerous factors. Proper radioisotope selection is the initial step. There is a wide variety of radionuclides used as positron emitters (Table 1). Physical half-life of the radioisotope will set limits on its use in molecular imaging. Short half-lived isotopes are usually preferred for in vivo applications to limit exposure. However, if physical half-life of the chosen isotope is too short, or mismatches the biological half-life of the nanoprobe, visualization of the target or process studied will not be achieved.

Table 1. Radioisotopes used in positron emission tomography (PET).

Radioisotope	Half-Life	Production Method
^{11}C	20.4 min	Cyclotron
^{13}N	9.97 min	Cyclotron
^{15}O	122 s	Cyclotron
^{18}F	110 min	Cyclotron
^{62}Cu	9.74 min	Cyclotron, Generator
^{64}Cu	12.7 h	Cyclotron
^{68}Ga	67.7 min	Cyclotron, Generator
^{76}Br	16.2 h	Cyclotron
^{82}Rb	76 s	Generator
^{89}Zr	78.4 h	Cyclotron
^{124}I	4.18 days	Cyclotron

By virtue of the outstanding sensitivity of nuclear imaging techniques, low concentration of the radionuclide is usually required. Hence, nanoparticle radiolabeling is expected to minimally alter nanoparticles' physicochemical properties and pharmacokinetics. Nevertheless, nanoparticle and radioisotope must form a chemically stable complex. Incorporating radioisotope to the nanoparticle will modify the core or the surface of the nanoparticle, depending on the radiolabeling strategy (Figure 1).

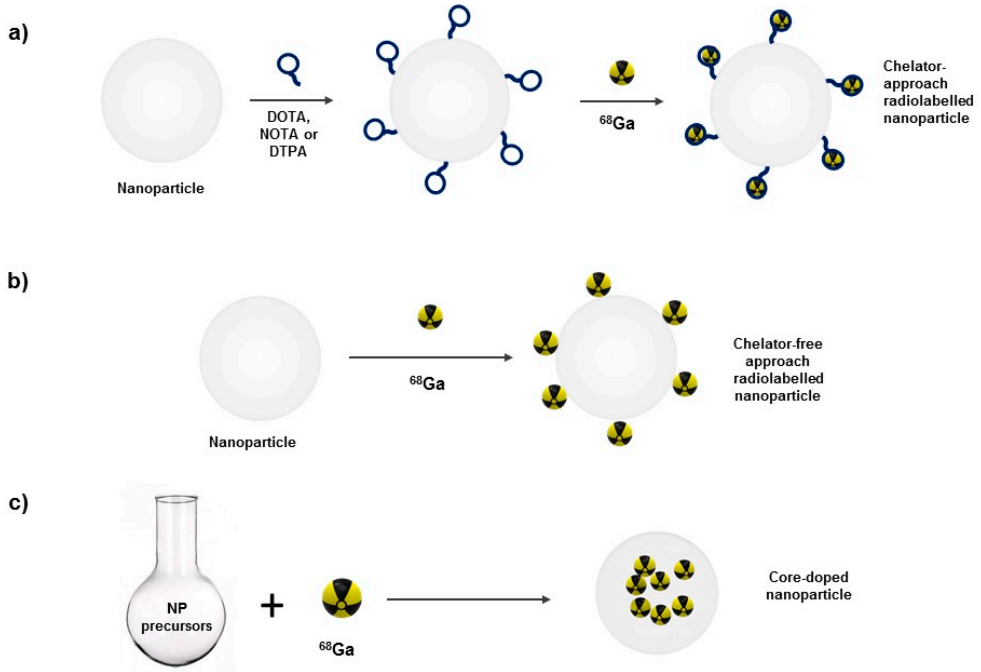

Figure 1. Nanoparticle radiolabeling approaches: (**a**) chelator approach; (**b**) chelator-free approach; and (**c**) nanoparticle core-doping. NP, nanoparticle; DOTA, 1,4,7,10-Tetraazacyclododecane-1,4,7,10- tetraacetic acid; NOTA, 1,4,7-triazacyclononane-1,4,7-trisacetic acid; DTPA, diethylenetriaminepentaacetic acid.

For this reason, radiolabeling strategy must be optimally designed to be fast and reproducible as well as to minimize potential radionuclide dissociation from nanoparticles [20].

Gallium, in aqueous solutions, is almost exclusively found in oxidation state +3, being highly influenced by pH. Optimal pH conditions range from pH 3 to pH 5. An excessively acidic media may protonate donor atoms and hence inhibit complex formation; and a neutral or basic environment may cause unreactive hydroxides formation.

3.1. Surface Radiolabeling

This procedure takes advantage of the increased surface-to-volume ratio of nanomaterials. This intrinsic property enables functionalization of the surface of the nanoparticles [63,64].

3.1.1. Chelator-Mediated Approach

This approach is a classical way to produce radiolabeled nanoparticles. Chelate ligands are conjugated to the surface of the nanoparticle to form a coordination complex between nanoparticle and radionuclide. It involves several steps: nanoparticle synthesis, functionalization with chelate ligand and radionuclide incorporation. Although this method demands multi-step protocols and purification steps, it endows nanoparticle functionalization prior to radiolabeling. Chelate ligand choice will depend upon several factors: stability of chelator–nanoparticle bond and stability of coordination complex between chelator and radionuclide. If chelator detaches from nanoparticle surface in vivo, PET signal will be derived from the chelator–radioisotope complex rather that from the radiolabeled

nanoparticle. Therefore, chelate ligand and nanoparticle are preferably attached by a covalent bond. Presence of different cations in the bloodstream (Ca^{2+} and Mg^{2+}) may trigger transmetallation reactions, displacing radioisotope in the coordination complex. Again, in this case, signal recovered will come from the free radioisotope and not from the nanoradiotracer.

Radioisotope choice determines chelate ligand used. Slower dissociation rates presented by macrocyclic ligands in comparison to their linear analogs bring about their preferential use. Common chelators for ^{68}Ga include a family of cyclic ligands based on heterocyclic N-dodecane or N-nonane moieties. Most commonly used ones are 1,4,7,10-tetraazacyclododecane-1,4,7,10-tetraacetic acid (DOTA); 1,4,7-triazacyclononane-1,4,7-triacetic acid (NOTA) and 1,4,7-triazacyclononane,1-glutaric acid-4,7-acetic acid (NODAGA). They have tetra- or triacetic acids that form extremely stable coordination complexes with ^{68}Ga (Figure 2).

Although it has not been yet used to radiolabel nanoparticles, Tris(hydroxypyridinone) (THP) has been used as ^{68}Ga chelator in vivo. Ma and coworkers used two THP conjugates, combined with the tumor-targeting peptide Arginine-Glycine-Aspartic (RGD), in murine models to detect U87MG tumors. They managed to radiolabel these conjugates with over 95% radiochemical yield under ambient conditions in less than 5 min, achieving activities ranging from 60 to 80 MBq·nmol^{-1} [65].

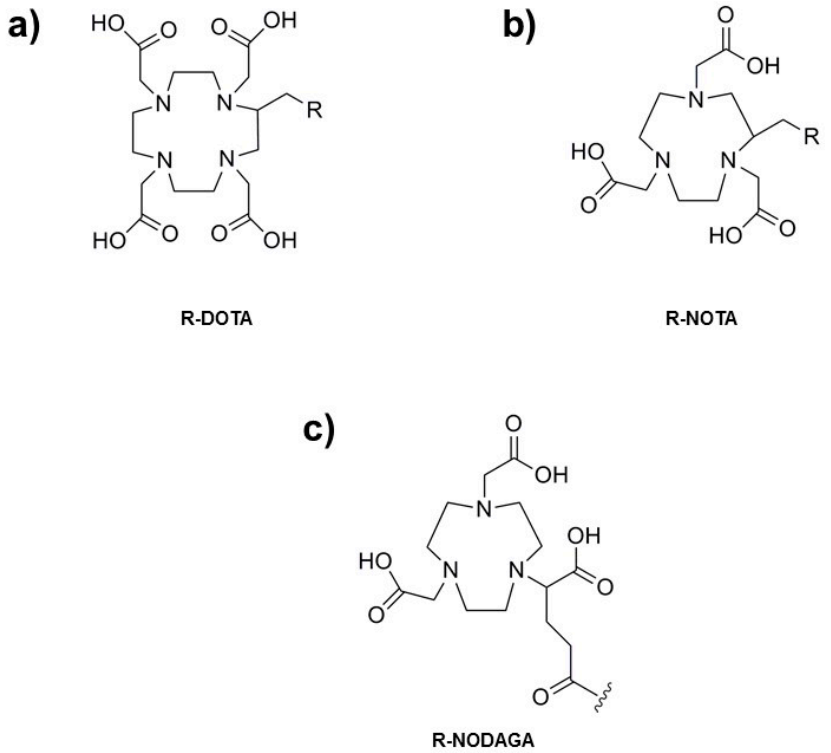

Figure 2. Most common ^{68}Ga chelators: (**a**) R-DOTA; (**b**) R-NOTA; and (**c**) R-NODAGA.

3.1.2. Chelator-Free Approach

In this radiolabeling strategy, the radioisotope is directly incorporated into the surface of the nanoparticle taking advantage of its affinity towards the nanoparticle surface. On the one hand, the major advantage is that the radioisotope can be incorporated to the nanoparticle in a single step. On the other hand, radioisotope desorption from nanoparticle surface is still the main drawback. Some examples in the literature have exploited this property to produce ^{68}Ge/^{68}Ga generators, to radiolabel nanoparticles with ^{69}Ge as well as to radiolabel iron oxide nanoparticles with several radioisotopes, including ^{68}Ga [8,66–70].

3.2. Nanoparticle Core-Doping

To overcome some of the limitations of surface labeling methods, intrinsic radiolabeling methods have been developed. Here, nanoparticle formation and radioisotope incorporation take place simultaneously [71]. Non-radioactive precursors and the radioisotope are combined to yield intrinsically radiolabeled nanoparticles. Optimal nanoparticle synthetic conditions and careful isotope selection ensure radioisotope incorporation within the core of the nanoparticle [32]. This prevents radioisotope desorption and transmetallation in vivo and confers increased radiochemical stability to the nanoradiotracer. A fast nanoparticle synthetic route is most suitable, as usually short half-lived isotopes are used. Therefore, reported examples of this methodology use microwave-assisted protocols to synthesize the core-doped iron oxide nanoradiotracers. In 2016, our group reported the synthesis of the first example of ^{68}Ga core-doped coated iron oxide nanoparticles for PET/MR imaging using microwave technology [72]. In a posterior study in 2017, the same approach was followed using citric acid as coating instead of dextran [73]. In 2016, Kandanapitiye et al. successfully incorporated ^{68}Ga to the crystalline structure of Prussian blue to form core-doped dual PET/MRI nanoparticles in a single step without the use of microwave technology, however did not try their potential as contrast agent in vivo [74].

4. Biomedical Applications of ^{68}Ga-Labeled Nanoparticles

Molecular imaging (MI) is defined as the ability to visualize and quantitatively measure the biochemical processes in a living organism at cellular and molecular level. Imaging techniques, such as optical imaging (OI), magnetic resonance imaging (MRI), magnetic particle imaging (MPI), computed tomography (CT), ultrasound (US), photoacoustic (PA), positron emission tomography (PET) and single photon emission computed tomography (SPECT), provide a deeper understanding of fundamental biological processes, allowing to relate their structure and function (Figure 3). Furthermore, MI enables longitudinal monitoring of subjects, facilitating long-term observations that allow elucidating specific behaviors, efficacy and failure causes of treatments.

Nevertheless, the need for improvement of spatial resolution along with the temporal resolution and the signal-to-noise ratio (SNR) of images has encouraged the development of innovative contrast agents. Research focusing on the use of nanomaterials in MI, for this purpose, has broadly increased during the past few years [75,76]. This growing interest can be explained by several factors involving nanoparticles exceptional properties. Firstly, due to their physical and chemical tailorability, these materials constitute highly flexible agents. Properties (size, shape, surface charge, etc.) governing critical parameters such as the pharmacokinetics of the probe or the ligand payload, can be easily customized. Secondly, given the available variety in their composition and size it is possible to produce probes for almost every imaging modality [77,78]. Finally, the intrinsic multifunctional character of most nanomaterials, greatly eases the performance of hybrid molecular imaging experiments. In this context, the radiolabeling of different NP types with ^{68}Ga seems an optimal approach for the development of multifunctional probes for hybrid imaging of diverse conditions and diseases (Table 2).

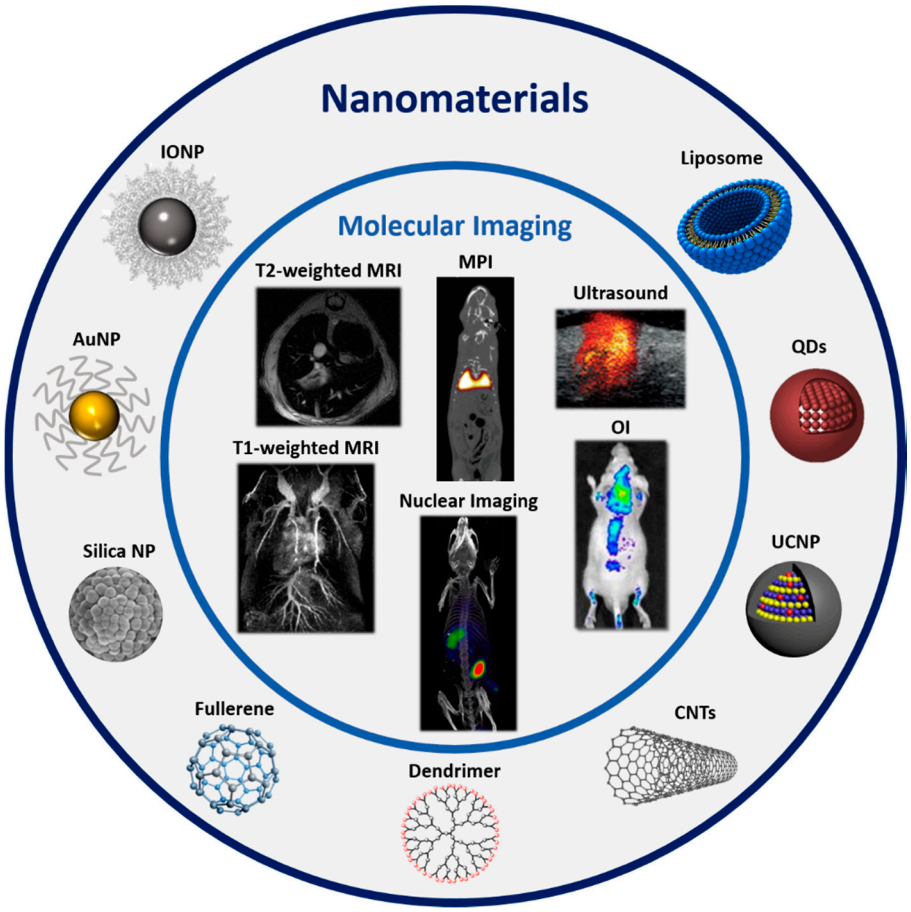

Figure 3. Different types of nanomaterials and the molecular imaging modalities to which they are applied. Ultrasound image adapted from Evertsson et al. [69], nuclear imaging image adapted from Lee et al. [79], Optical Imaging (OI) image adapted from Zheng, M. et al. [80], Magnetic Particle Imaging(MPI) image adapted from Zheng, B. et al. [81].

4.1. Iron Oxide Nanoparticles (IONPs)

Iron oxide nanoparticles (IONPs) have been broadly used as imaging probes [82]. Their size-dependent MRI properties together with their superparamagnetic behavior, biocompatibility and chemical stability place them as a particularly important NP type for biomedical applications [83]. IONPs are typically composed of magnetite (Fe_3O_4) and/or maghemite (γ-Fe_2O_3) nanocrystals, which may exhibit different shapes (spheres, cubes, rods, rings, flowers, pyramids, etc.). Regarding coating molecules, the most commonly used ones are organic polymers, such as polyethylene glycol (PEG), oleic acid, dextran, chitosan, phospholipids, and other amphiphilic polymers.

As tracers for molecular imaging, IONPs are most commonly used for MRI. Due to their superparamagnetic behavior they have been mainly used for T_2-weighted MRI, therefore producing a darkening effect on the tissue surrounding them [84–86]. Nevertheless, several disease conditions, such as bleeding or calcifications, create an endogenous hypointense signal that makes IONPs indistinguishable from biological tissue. This drawback has focused research on finding methods for developing IONPs that serve as positive contrast agents for T_1-weighted MRI. Studies have demonstrated that the downsizing of IONP core or coating thickness causes a shift on the NP magnetic behavior from superparamagnetic towards paramagnetic, thus creating T_1-weighted MRI contrast agents [72,87–89].

Additionally, IONPs are being used as a contrast agent in a novel technique that has gained strength in the research field during the past few years, Magnetic Particle Imaging (MPI) [90]. MPI can

visualize superparamagnetic iron oxide (SPIO) tracers by direct induction, meaning MPI signal increases linearly with the amount of SPIO present in the imaged volume. Given this, MPI can be seen as a "hotspot" imaging technique with no background signal, similar to nuclear imaging techniques but without ionizing radiation. In addition, unlike OI, ultrasound, X-ray, and other imaging methods, its magnetic signal suffers zero attenuation with depth. However, the lack of anatomical information from this technique implies it cannot be used as a single imaging modality, again similarly to nuclear imaging techniques. This technique is still in its infancy; however, it has tremendous potential to surpass some of the limitations of IONPs in MRI without the inconvenience associated to nuclear imaging techniques. Several research groups have already demonstrated the capability of MPI to track stem cells in small-animal models systemically and longitudinally [81,91,92]; and to visualize brain and tumor vasculature for potential diagnosis of stroke and cancer, using SPIO nanoparticles [78,93] (Figure 4).

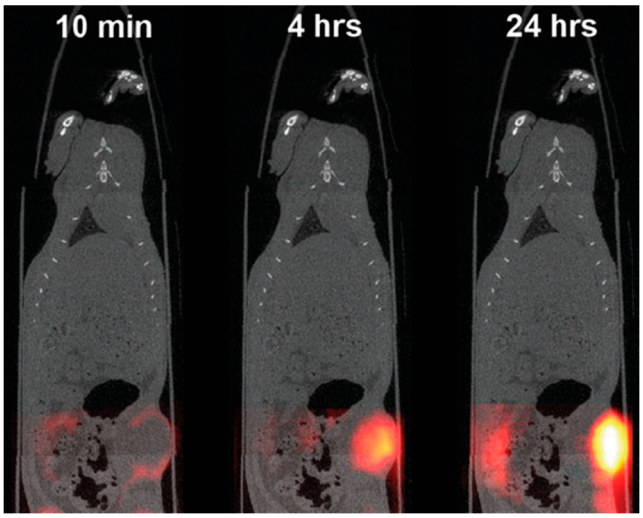

Figure 4. In vivo MPI/CT image of a human breast tumor in a murine model, using SPIO nanoparticles specifically designed for MPI [94]. SPIO nanoparticles can be observed to accumulate in tumor having a contrast peak at 24 h post injection. Adapted from Zheng et al. [78].

In addition to these single imaging modalities, IONPs have been reportedly used as probes for multimodal PET/MRI imaging. With the fusion of these two techniques PET imaging takes advantage of the excellent soft tissue contrast resolution and pathological discrimination offered by MRI, overcoming its lack of anatomical detail. To provide signal in PET, IONPs have been radiolabeled with different radioisotopes such as ^{64}Cu [5–7,95], ^{68}Ga [70,72,96–99], ^{18}F [2–4], ^{124}I [12,13], ^{11}C [17], and ^{89}Zr [100].

IONP-based ^{68}Ga nanoradiotracers have been assessed in preclinical models to ensure biocompatibility and study in vivo biodistribution. Lahooti et al. [101] radiolabeled PEG-coated iron oxide nanoparticles with ^{68}Ga using a chelator-free strategy previously described by Madru et al. [70], incubating IONPs with $GaCl_3$ eluate for 30 min at room temperature. They obtained a 66.2% post labeling chemical purity that improved to 98.9% after magnetic separation nanoparticle purification (using a MACS column). In vivo PET imaging in mice revealed fast blood clearance and major liver and spleen nanoparticle accumulation. This biodistribution profile is typical for numerous nanoparticulate-based tracers, as they are mainly eliminated by the reticuloendothelial (RES) organs. RES is part of the immune system of the body, being a network of cells and tissues, especially in the blood, general connective tissue, spleen, liver, lungs, bone marrow, and lymph nodes. These varied cell types which acted in host defense by phagocytosing of foreign invaders such as microbes are grouped collectively into the RES. Nanoradiotracers smaller than ~5 nm will be able to leak through renal

glomeruli and excreted via urinary system [102]. However, if nanoradiotracer has a larger size, they will interact with immune blood components, as for instance opsonins. This eases nanoradiotracer recognition by Kupffer cells, which are a macrophage type resident in the liver. These will capture nanoradiotracer via endocytosis and process nanoparticles in their lysosomes, in the case of iron oxide nanoparticles, to release free iron that will become part of the physiological iron reservoirs in the form of ferritins and hemosiderins [103,104]. These will have no impact in homeostasis when nanoradiotracer is administered at suitable concentrations. The spleen is also a host organ for macrophages that phagocyte the nanoradiotracer. This explains biodistribution trend followed by a great number of untargeted nanoradiotracers. Locatelli et al. [98] entrapped maghemite nanoparticles in a polymeric matrix composed by PLGA and PEG and radiolabeled them with ^{68}Ga using NODAGA as a chelator. NODAGA was incorporated to the surface of the nanoparticles via peptide bond formation with an amine coming from NODAGA-ethylenediamine and a polyCOOH-containing organic shell on nanoparticle surface. Radiolabeling yield obtained with ^{68}Ga was 84%. In vivo PET imaging and time–activity curves for different organs pointed towards a slow blood clearance pattern and high accumulation in liver and spleen. They also observed significant accumulation in the lungs, suggesting nanoparticle clustering or aggregation. Karageorgou et al. [105] obtained a dual PET/MRI nanoradiotracer composed by iron oxide nanoparticles conjugated to DPD, a tetradentate ligand (with two phosphonates and two carboxylate groups) that apart from acting as surfactant, serves as ^{68}Ga chelator. They obtained a 70% radiolabeling yield and a >91% chemical purity. In vivo PET imaging and ex vivo biodistribution studies in Swiss mice showed high accumulation in liver and spleen. Burke et al. [106] described a new class of silica-coated iron oxide nanorods radiolabeled with ^{68}Ga in a chelator-free manner via surface interactions. Radiolabeled construct stability was assessed incubating it with human serum at physiological conditions. After 3 h, 95% of ^{68}Ga remained attached to nanoconstructs, denoting complex was highly stable. PET and MR imaging revealed liver accumulation of the probe.

Lymph nodes play a key role in cancer cell metastasis; hence the development of probes capable of targeting and visualizing these structures, has become the main focus of several study groups. Madru et al. [70] developed chelator-free ^{68}Ga-labeled SPIONs. To radiolabel their SPIONs, they incubated $GaCl_3$ with SPIONs in 1M acetate buffer pH 5.5 for different times to assess the best fitting one. They obtained 95% radiolabeling efficiency within 10 min and managed to achieve 97.3% after 15 min of incubation. ^{68}Ga-labeled SPIONs proved to be stable in human serum at 37 °C for 4 h. These SPIONs served as a dual probe for PET/MR imaging of Sentinel Lymph Nodes (SLN), the first node receiving lymphatic drainage from the primary tumor site, in rat models (Figure 5). Evertsson et al. [69] utilized Madru and coworkers' [70] ^{68}Ga-SPIONs as a contrast agent for magnetomotive ultrasound (MMUS); a novel ultrasound-based method for intra-surgical guidance to localize metastases during cancer surgery. In their study, ^{68}Ga-SPIONs served as a dual-imaging probe for pre-operative PET/MRI imaging followed by intra-operative MMUS imaging in a SLN rat model. Yang et al. [99] used amphiphile-encapsulated iron oxide nanoparticles, radiolabeled with ^{68}Ga using NOTA chelate ligand, to monitor lymph node uptake via PET and T_2-weighted MR imaging. High radiochemical yield was obtained (<95%) and stability in human serum was tested in human serum by gel filtration at 37 °C, suggesting nanoparticles are stable in human serum under physiological conditions.

Over the last few decades, numerous discoveries have enlightened molecular bases of cancer. This in conjunction with the lack of implementations to study molecular events in depth has motivated the quest for novel approaches in cancer detection. Several groups have focused on the development of radiolabeled nanoprobes for the detection of this disease. Passive accumulation of nanoradiotracers in tumors, due to enhanced permeability and retention (EPR) effect, has been widely used as a delivery strategy to locate carcinogenic tissue [6,107,108]. EPR effect is the increased permeation of blood vessels to tumor interstitial space, surrounding tumor environments. They allow delivery and retention of drugs and imaging agents with moderated specificity [109,110].

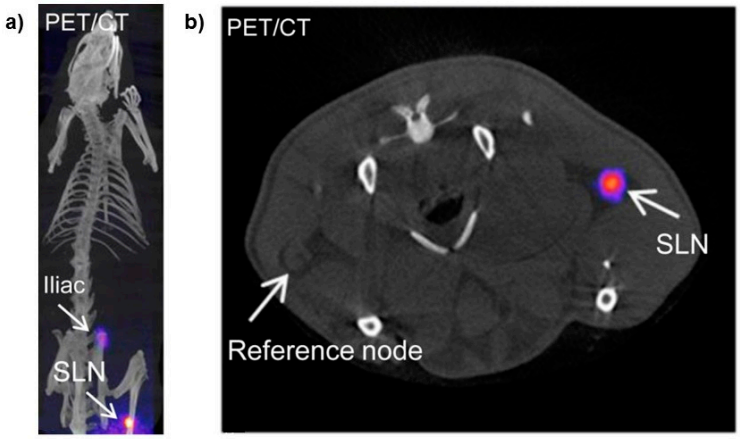

Figure 5. (**a**) PET/CT imaging 3 h post subcutaneous injection of ^{68}Ga-SPION. Arrow shows nanoparticle accumulation in SLN (popliteal) and iliac nodes; and (**b**) axial PET/CT slice 3 h post subcutaneous injection of ^{68}Ga-SPION. Arrows point SLN and reference nodes. Adapted from Madru et al. [70].

Even though passive accumulation of NPs in the tumor site has proven to be a valuable method for imaging angiogenesis, active targeting of cancerous cells by means of tumor targeting moieties substantially increases probe specificity providing better quality images. Kim et al. [96] conjugated PEG-coated ^{68}Ga-NOTA-IONPs with oleanolic acid (OA), a novel tumor targeting molecule, to specifically target HT-29 cancer cells in a murine model [32]. Functional amines in PEG coating enabled tumor targeting moiety (oleanolic acid) and chelating agent for ^{68}Ga (NOTA) incorporation. With this approach, they could visualize the xenograft tumor in vivo using PET/MRI imaging. Furthermore, Moon et al. [97] developed prostate-specific membrane antigen (PSMA) targeting IONPs for in vivo PET and MR imaging of mouse prostate cancer xenograft models, revealing specific accumulation in tumor site. For this purpose, IONPs were encapsulated with amphiphiles containing PEG, DOTA and glutamate-urea-lysine (GUL), the PSMA targeting ligand; and subsequently radiolabeled with ^{68}Ga obtaining 99% efficiency. Radiochemical purity of the final radiolabeled nanoprobe was higher than 99%. Pellico et al. [72] obtained via microwave-assisted synthesis a core-doped hybrid nanoradiotracer, ^{68}Ga core-doped dextran-coated IONPs, that was posteriorly conjugated to RGD peptide via 1,4-(butanediol) diglycidyl ether homobifunctional crosslinker, to target angiogenesis in a subcutaneous melanoma murine model. To core dope the nanoparticles, $^{68}GaCl_3$ eluate was added to initial precursors and mixture introduced into the microwave for 10 min at 100 °C. Radiolabeling yield obtained was 93.4%. In vivo PET and T_1-weighted MRI experiments confirmed specific tumor accumulation of the ^{68}Ga-C-IONP-RGD probe. In a posterior study performed by Pellico et al. [73], an analogous iron oxide-based tracer was synthesized following the same procedure previously described, using citrate as a surfactant instead of dextran. Radiolabeling yield obtained was 92%. Nanoradiotracer was functionalized with a highly hydrophobic neutrophil-specific peptide, N-cinnamoyl-F-(D)L-F-(D)L-F (c-FLFLF), to visualize inflammation processes in vivo. Functionalized nanoradiotracer was injected in vivo in acute lung inflammation and chronic inflammation murine models. PET imaging revealed high in vivo labeling efficiency of the nanoradiotracer and yielded high quality images of neutrophil recruitment. Probe specificity for neutrophils, was checked using a neutrophil-depleted model (Figure 6).

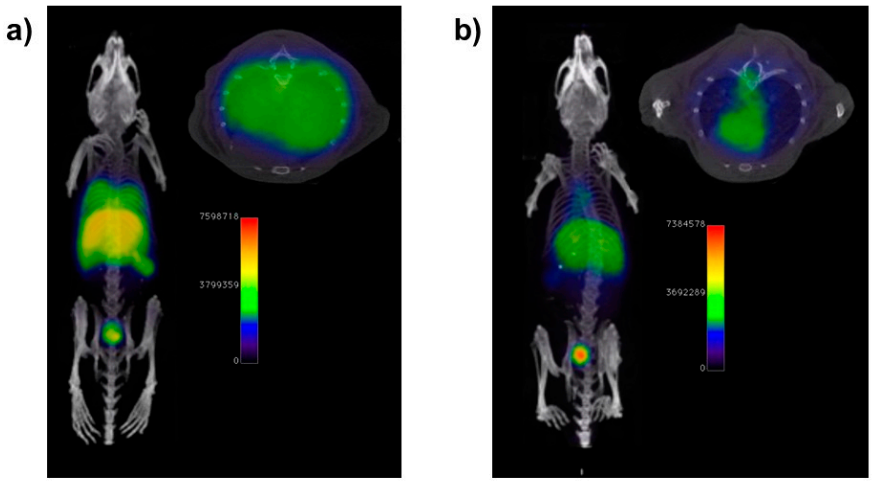

Figure 6. (**a**) PET/CT imaging of a mouse with LPS-induced lung inflammation 1 h post i.v. injection of ^{68}Ga nanoradiotracer functionalized with N-cinnamoyl-F-(D)L-F-(D)L-F (cFLFLF). Neutrophil recruitment in the lungs is clearly observed. (**b**) PET/CT image of a neutrophil-depleted, LPS-treated mouse 1 h post i.v. injection of ^{68}Ga nanoradiotracer functionalized with cFLFLF. Adapted from Pellico et al. [73].

4.2. Liposomes

Liposomes are probably the most used nanomaterial in nanomedicine for research and clinical applications. Liposomes are spherical vesicles consisting on amphiphilic phospholipids (e.g., phosphatidylcholine, phosphatidyl-ethanolamine, phosphatidylserine and phosphatidyl-glycerol) that form a lipid bilayer enclosing an aqueous core. This structure allows the encapsulation of both hydrophobic and hydrophilic molecules, which provide diverse and tunable properties to the nanoplatform.

Primarily, liposomes have been studied as drug delivery agents [111–114]; nevertheless, increased attention has been brought to the development of multifunctional liposomes as theranostic agents. With this kind of platforms, diagnosis and treatment can be achieved simultaneously. For this purpose, liposomes are either labeled or loaded with both, the therapeutic agent and the imaging probe. Visualization of liposomes with T_1-weighted MRI [115,116] and T_2-weighted MRI [117], PET [118–120] and OI [121], among others, has been achieved in several studies.

Helbok et al. [122] compared radiolabeling PEGylated-DTPA liposomes using different radiometals: ^{111}In, ^{99m}Tc for SPECT; ^{68}Ga for PET and ^{177}Lu for therapeutic applications. DTPA served as chelate ligand on the surface of the liposomes. ^{68}Ga radiolabeling of these nanoparticles was achieved with 98% radiochemical yield. In vivo fate of this nanoradiotracer was evaluated in Lewis rats, showing modest blood circulation time. Fused PET/MR images acquired 20 min revealed major liver and spleen accumulation. Malinge et al. [119] synthesized DSPE-PEGylated liposomes loaded with maghemite nanoparticles in their lumen in order to perform magnetic targeting and use them as MRI contrast agents. They incorporated glucose in the lipid formulation as an extra tumor-targeting moiety. Liposomes were radiolabeled with ^{68}Ga using NODAGA as chelating agent; obtaining low radiolabeling yields (10%) at room temperature, but reaching 70% radiolabeling yield at 80 °C. These nanoradiotracers were injected through the retro-orbital sinus of U87MG tumor-bearing mice. They compared probe accumulation in the tumors with and without the use of magnetic targeting; and with and without glucose moiety in the liposome formulation. PET images acquired 30 min post-injection reveal increased nanoradiotracer accumulation in those with magnetic targeting. Effect of glucose targeting showed contradictory results, as MRI showed positive results that resulted non-significant with PET and ex vivo quantification (Figure 7).

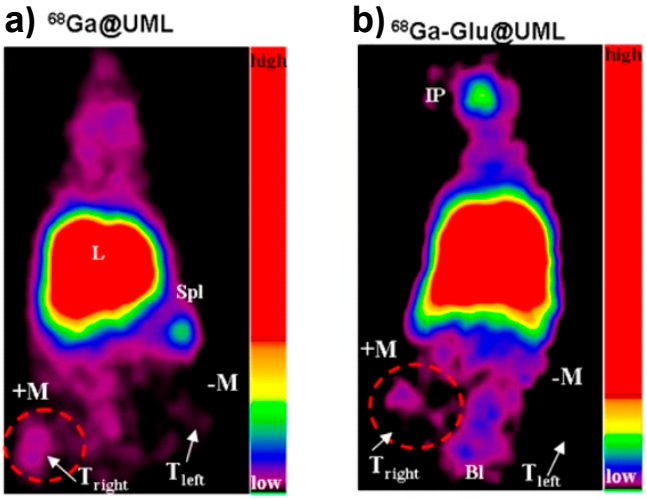

Figure 7. (**a**) PET image 30 min post ^{68}Ga radiolabeled liposome injection (without glucose in the formulation); and (**b**) PET image 30 min post ^{68}Ga radiolabeled glucose liposome injection. The arrows show tumors. IP, injection point; K, kidneys; L, liver; Spl, spleen; Bl, bladder; M, magnet; T_{right} and T_{left}, tumors. Adapted from Malinge et al. [119].

4.3. Nanoparticles for Optical Imaging

OI is limited by tissue penetration from photon attenuation due to the absorption and scattering properties of tissues. However, the revelation of the tissue transparent window in the infrared region within 700–2000 nm has encouraged the development of fluorescent probes that can support real-time, tissue specific and multispectral fluorescent imaging methods [123].

4.3.1. Quantum Dots

QDs possess unique size-dependent photo luminescent properties due to the quantum confinement effect [124–126]. They produce bright emissions spanning the visible and infrared spectrum when excited by high-energy photons. QDs are composed by hundreds to thousands of atoms from group II and VI elements (e.g., CdSe and CdTe) or group III and V elements (e.g., InP and InAs). Their size and shape (dots, rods or tetrapods) [127], together with their internal structure (core-shell, gradient alloy or homogeneous alloy) can be precisely controlled [128]. Among the studied types of QDs the core-shell configuration of CdSe/ZnS has been shown to yield the best performance, having been used for several in vitro and in vivo studies [129–131].

However, due to the known toxic effect that heavy metals contained in this type of NPs have in vivo, research has been focused on their biocompatible quantum-sized carbon analogs, carbon dots (CDs) [80,132]. CDs are formed by small carbon molecules that are surface-passivated by organic molecules or biomolecules becoming strongly fluorescent in the visible and near-infrared (NIR) spectral regions. Several research groups have carried out studies using CDs to produce OI in vivo [133,134].

Fazaeli et al. [135] radiolabeled CdTe quantum dots using heteroleptic chelated-carboxylatogallium(III) stable complexes, –SCH_2(CO)CO– was used as chelate ligand to complex QDs to ^{68}Ga. Nanoradiotracer radiochemical purity was maintained at 99% during the first 5 h. They were used in vivo for fibro sarcoma coincidence imaging in tumor-bearing rats. Coincidence imaging during the 40 first minutes after nanoradiotracer injection revealed significant tumor and liver accumulation. Ex vivo gammacounter quantification 30 min, 1 h and 2 h post injection confirmed probe accumulation was five times higher in tumor than in liver, blood, kidneys and lungs.

4.3.2. Upconverting Nanoparticles

Rare-earth upconverting nanoparticles (UCNPs) constitute another probe widely used for OI [136,137]. Most of the conventional fluorescent probes for bioimaging, including QDs, are based on single-photon excitation, emitting low energy fluorescence when excited by high energy light. Consequently, images produced by this type of probes possess low SNR caused by significant auto-fluorescence from biological tissues. Furthermore, due to the high energy excitation light, the penetration depth in biological tissues is poor. UCNPs emerged as an alternative aiming to cast out these limitations. Upconversion luminescence (UCL) is a unique process where low-energy light, usually NIR light, is converted into higher energy light through the sequential absorption of multiple photons or energy transfers [138]. Upon a continuous wave (CW) excitation at 980 nm UCNPs, in particular lanthanide (Ln)-doped UCNPs, exhibit unique UCL properties, such as long lifetimes, high photostability and sharp emission lines that can be multiple when doped with several lanthanides (Figure 8) [139].

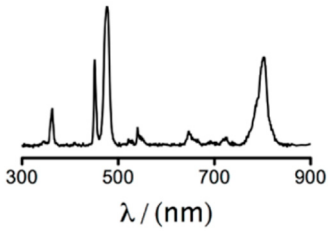

Figure 8. Fluorescence emission spectrum for UCNPs doped with several lanthanides after excitation with CW laser at 980 nm [139]. Multiple emission peaks can be observed at 360 nm, 451 nm, 476 nm and 800 nm.

The unique properties provided by UCL makes UCNPs truly advantageous for in vivo luminescence imaging. Firstly, due to the low harm that infrared excitation produces in tissues. Secondly, due to the lack of autofluorescence from biological samples, since they do not produce UCL under CW excitation at 980 nm. Finally, due to the increase in SNR, which produces high imaging contrast. For these reasons, research focusing on in vivo OI with UCNPs has been growing throughout the past years [140]. Furthermore, these UCNPs can be used in photoacoustic imaging, expanding their application field [141].

In addition to their use in OI, several examples of multimodal UCNPs have been developed. Gd^{3+} doped UCNPs have been used for T_1-MRI [142–144]. Moreover, the high X-ray attenuation of Lanthanide elements has been exploited for the use of UCNPs as CT contrast agents [145,146]. Finally, ^{18}F-labeled UCNPs were synthesized for PET imaging [147].

Concerning the use of these type of nanoparticles with ^{68}Ga, Gallo et al. [148] labeled UCNPs via DOTA chelator with this isotope and conjugated them to RGD peptide to accomplish targeted visualization of tumor integrin $\alpha_v\beta_3$ expression in M21 tumor bearing mice using RGD peptide as targeting moiety. Amines in the surface of the UCNPs reacted with DOTA-NHS to attach DOTA to UCNPs. RGD functionalization took place using SPDP heterobifunctional crosslinker. Different radiolabeling pH conditions were tried. Highest radiolabeling percentage of UCNPs was obtained at pH 6 (87.5%), however they selected pH 5 as, above pH 6.3, Ga^{3+} forms $Ga(OH)_3$ which is insoluble in water. Radiolabeling yield at pH 5 was 15.2% for the targeted UCNPs. Accumulation at tumor site of ^{68}Ga-labeled UCNPs was confirmed by PET imaging and ex vivo quantification.

4.4. Other Nanoparticles

Besides the above mentioned nanoprobes, many other nanoparticle types have been developed for MI. Examples of these include Au nanoparticles [149,150], dendrimers [151,152], carbon nanotubes [153,154], or silica nanoparticles [155,156].

Frigell et al. [157] developed glucose-coated gold nanoparticles radiolabeled with ^{68}Ga via NOTA ligand, functionalized with opioid-related peptides to improve BBB crossing. NOTA was functionalized with linkers containing a thiol-ending group to attach the chelator to the gold surface. ^{68}Ga incorporation efficiencies obtained range from 85 to 94% within 30 min and 70 °C. In vivo PET imaging and ex vivo quantification in rats revealed different biodistribution patterns that depend on peptides with which nanoparticles were functionalized. Only nanoparticles functionalized with Leu-enkephalin peptide revealed improved brain accumulation.

Ghai et al. [108] took advantage of the EPR effect in cancerous tissue vasculature to visualize Ehrlich's ascites tumors in Balb/c mice. They radiolabeled generation four polyamido-amine dendrimers (G4-PAMAM-D) with ^{68}Ga via DOTA-NHS chelator, achieving more than 93% radiolabeling efficiency. Dendrimer-based nanoprobe remained stable in serum at room temperature up to 4 h. Passive probe accumulation at tumor site was confirmed using PET imaging.

Truillet et al. [158] synthesized a nanoradiotracer composed by a polysiloxane matrix scaffold surrounded by DOTAGA[Gd^{3+}] and NODAGA[$^{68}Ga^{3+}$] for PET/MRI. NODAGA and DOTAGA were grafted onto the NP shells by amide bond formation between activated NHS groups of NODAGA and anhydride function of DOTAGA and the amino groups in shell. Nanoparticles were successfully radiolabeled with a high radiochemical purity (>97%) and were stable up to 3 h. They injected them in vivo in Swiss mice and observed fast renal clearance after retro-orbital injection. Bouziotis et al. [107] made use of this same nanoradiotracer to prove its successful passive accumulation in mouse xenograft tumor models of U87MG human glioblastoma, via PET and MRI imaging, thus demonstrating its usefulness as a cancer imaging agent. Serum metabolite assessment in urine, serum and tumor samples proved nanoprobe remained unmetabolized up to 60 min post-injection.

Polyak et al. [159] prepared ^{68}Ga-labeled porous zirconia nanoparticles using DOTA as chelating ligand. DOTA was adsorbed on the surface of zirconia nanoparticles. Radiolabeling showed high efficiency (90.5–97.5%) and they were stable in HEPES and human blood serum. They tested biodistribution in vivo in mice. PET imaging after intravenous probe injection revealed major liver and spleen nanoradiotracer accumulation.

Shaffer et al. [160] radiolabeled silica nanoparticles with several radiometals using a chelator free approach, incorporating cations in the pores of the nanoparticles. ^{68}Ga was successfully incorporated to the nanoparticles with 99% radiolabeling yield. They assessed nanoprobe biodistribution in vivo in athymic nude mice and compared it to the biodistribution of free ^{68}Ga. PET images acquired 1 and 3 h post injection reveal nanoprobe mainly accumulates in liver and spleen, whereas free gallium presented an entirely different biodistribution profile, with the bladder as major organ eliminating free ^{68}Ga.

Cartier et al. [161] labeled poly2,3-epoxypropylmethacrylate (EPMA) latex nanoparticles in a chelator-free manner with Gd^{3+} for MRI, ^{111}In for gamma scintigraphy or ^{68}Ga for PET imaging. ^{68}Ga nanoradiotracer was obtained with 0.2 MBq/mg nanoparticles. It was posteriorly injected in Wistar rats to assess biodistribution using PET imaging. Fifteen minutes post-injection, one can mainly observe liver, spleen and heart accumulation.

Table 2. Examples of the combined use of nanomaterials and ^{68}Ga. MRI: magnetic resonance imaging; MMUS: magnetomotive ultrasound; CT: computed tomography.

Nanomaterial	Radiolabeling Method	Imaging Modalities	Biomedical Application	Reference
Fe_3O_4-PEG	Surface labeling. Chelator-free	PET/MRI	Biodistribution studies	[101]
γ-Fe_2O_3-PLGA-PEG	Surface labeling. Chelator approach (NODAGA)	PET/MRI	Biodistribution studies	[98]
Fe_3O_4-DPD	Surface labeling. Chelator approach (DPD)	PET/MRI	Biodistribution studies	[105]
γ-Fe_2O_3-citrate-cFLFLF peptide	Core doping	PET/MRI	Neutrophil recruitment imaging in lung inflammation	[73]
Fe_3O_4-PEG-GUL peptide	Surface labeling. Chelator approach (DOTA)	PET/MRI	Prostate tumor imaging	[97]
γ-Fe_2O_3-dextran-RGD peptide	Core doping	PET/MRI	α_v β_3 integrin expression imaging in melanoma	[72]
Fe_3O_4-PEG	Surface labeling. Chelator free	PET/MRI/Cherenkov	Sentinel lymph node imaging	[70]
Fe_3O_4-PEG	Surface labeling. Chelator free	PET/MRI/MMUS	Sentinel lymph node imaging	[69]
Fe_3O_4-mannose	Surface labeling. Chelator approach (NOTA)	PET/MRI	Sentinel lymph node imaging	[99]
Fe_3O_4-PEG-Oleanolic acid	Surface labeling. Chelator approach (NOTA)	PET/MRI	HT-29 cancer cell tumor imaging	[96]
Iron oxide nanorods-Silica-PEG	Surface labeling. Chelator free	PET/MRI	Biodistribution studies	[106]
DSPE-PEG-Glucose liposomes	Surface labeling. Chelator approach (NODAGA)	PET/MRI	U87MG glioblastoma imaging	[119]
DTPA-PLP PEGylated liposomes	Surface labeling. Chelator approach (DTPA)	PET/MRI	Biodistribution studies	[122]
CdTe	Surface labeling. Chelator approach (–SCH_2(CO)CO–)	Coincidence imaging (Optical)	Fibro sarcoma imaging	[135]
$NaYF_4$-PEG-RGD peptide	Surface labeling. Chelator approach (DOTA)	PET/CT	M21 tumor imaging	[148]
Polysiloxane matrix-[Gd-DOTA] (AGuIX)	Surface labeling. Chelator approach (NODAGA)	PET/MRI	Biodistribution studies	[158]
Polysiloxane matrix-[Gd-DOTA] (AGuIX)	Surface labeling. Chelator approach (NODAGA)	PET/MRI	U87MG glioblastoma imaging	[107]
ZrO_2	Surface labeling. Chelator approach (DOTA)	PET/CT	Biodistribution studies	[159]
Dendrimers (G4-PAMAM-D)	Surface labeling. Chelator approach (DOTA)	PET/CT	Ehrlich's ascites tumor imaging	[108]
Au-glucose-opioid related peptides	Surface labeling. Chelator approach (NOTA)	PET/CT	Blood brain barrier permeability imaging	[157]
Silica	Surface labeling. Chelator free	PET	Biodistribution studies	[160]
EPMA latex	Surface labeling. Chelator free	PET/MRI	Biodistribution studies	[161]

5. Prospects and Conclusions

The combined use of radioisotopes and nanomaterials is already a mature field with numerous examples on their use in molecular imaging. The combination of chemical and physical properties with aspects more related to the logistics of the daily work (production, waste management, etc.) make of ^{68}Ga a "user friendly" isotope. This is translating onto many applications at both preclinical and clinical levels. As we have seen, the variety of radioisotope-nanomaterial combination is quite large and with enormous potential. The advantages of this combined approach are manifold and affects both the nanomaterial and the radioisotope. For example, the detailed and quantitative study of nanoparticle biodistribution is greatly improved with the use of nuclear techniques. Accounting for all the injected nanomaterial with other techniques is a hard task, if possible at all; however, it is relatively easy using techniques such as PET or gammacounter data. On the other hand, the addition of the size-dependent properties typical of nanomaterials to a classical radiotracer has numerous advantages: the possibility of easily tuning the pharmacokinetics of the tracer, the use of multimodal imaging techniques and the addition of a drug to the radio-nanomaterial for theranostics experiments, among others. All things considered, we believe the combined use of ^{68}Ga and nanomaterials is full of exciting possibilities that will improve the field of biomedical imaging at preclinical and clinical levels.

Author Contributions: I.F.-B. planned and wrote Sections 3–5. M.M.-H. planned and wrote Sections 2 and 5. J.P. and F.H. planned and wrote Sections 1 and 5 and supervised the work. J.R.-C. supervised the work and provided technical advice. All co-authors contributed to the final version with suggestions and critical comments.

Funding: We thank Ministerio de Economía, Industria y Competitividad (MEIC) for financial support (SAF2016-79593-P) and Instituto de Salud Carlos III (DTS16/00059).

Acknowledgments: The CNIC is supported by MEIC and the Pro CNIC Foundation, and is a Severo Ochoa Center of Excellence (SEV-2015-0505).

Conflicts of Interest: The authors declare no conflict of interest.

References

1. Abou, D.S.; Pickett, J.E.; Thorek, D.L.J. Nuclear molecular imaging with nanoparticles: Radiochemistry, applications and translation. *Br. J. Radiol.* **2015**, *88*, 20150185. [CrossRef] [PubMed]
2. Devaraj, N.K.; Keliher, E.J.; Thurber, G.M.; Nahrendorf, M.; Weissleder, R. 18F Labeled Nanoparticles for in Vivo PET-CT Imaging. *Bioconjug. Chem.* **2009**, *20*, 397–401. [CrossRef] [PubMed]
3. Nahrendorf, M.; Keliher, E.; Marinelli, B.; Leuschner, F.; Robbins, C.S.; Gerszten, R.E.; Pittet, M.J.; Swirski, F.K.; Weissleder, R. Detection of Macrophages in Aortic Aneurysms by Nanoparticle Positron Emission Tomography-Computed Tomography. *Arterioscler. Thromb. Vasc. Biol.* **2011**, *31*, 750–757. [CrossRef] [PubMed]
4. Sun, Z.; Cheng, K.; Wu, F.; Liu, H.; Ma, X.; Su, X.; Liu, Y.; Xia, L.; Cheng, Z. Robust surface coating for a fast, facile fluorine-18 labeling of iron oxide nanoparticles for PET/MR dual-modality imaging. *Nanoscale* **2016**, *8*, 19644–19653. [CrossRef] [PubMed]
5. Glaus, C.; Rossin, R.; Welch, M.J.; Bao, G. In Vivo Evaluation of 64 Cu-Labeled Magnetic Nanoparticles as a Dual-Modality PET/MR Imaging Agent. *Bioconjug. Chem.* **2010**, *21*, 715–722. [CrossRef] [PubMed]
6. Xie, J.; Chen, K.; Huang, J.; Lee, S.; Wang, J.; Gao, J.; Li, X.; Chen, X. PET/NIRF/MRI triple functional iron oxide nanoparticles. *Biomaterials* **2010**, *31*, 3016–3022. [CrossRef] [PubMed]
7. Yang, X.; Hong, H.; Grailer, J.J.; Rowland, I.J.; Javadi, A.; Hurley, S.A.; Xiao, Y.; Yang, Y.; Zhang, Y.; Nickles, R.J.; et al. CRGD-functionalized, DOX-conjugated, and 64Cu-labeled superparamagnetic iron oxide nanoparticles for targeted anticancer drug delivery and PET/MR imaging. *Biomaterials* **2011**, *32*, 4151–4160. [CrossRef] [PubMed]
8. Chakravarty, R.; Valdovinos, H.F.; Chen, F.; Lewis, C.M.; Ellison, P.A.; Luo, H.; Meyerand, M.E.; Nickles, R.J.; Cai, W. Intrinsically Germanium-69-Labeled Iron Oxide Nanoparticles: Synthesis and In-Vivo Dual-Modality PET/MR Imaging. *Adv. Mater.* **2014**, *26*, 5119–5123. [CrossRef] [PubMed]

9. Xue, S.; Zhang, C.; Yang, Y.; Zhang, L.; Cheng, D.; Zhang, J.; Shi, H.; Zhang, Y. 99mTc-Labeled Iron Oxide Nanoparticles for Dual-Contrast (T1/T2) Magnetic Resonance and Dual-Modality Imaging of Tumor Angiogenesis. *J. Biomed. Nanotechnol.* **2015**, *11*, 1027–1037. [CrossRef] [PubMed]
10. Morales-Avila, E.; Ferro-Flores, G.; Ocampo-García, B.E.; De León-Rodríguez, L.M.; Santos-Cuevas, C.L.; García-Becerra, R.; Medina, L.A.; Gómez-Oliván, L. Multimeric system of 99mTc-labeled gold nanoparticles conjugated to c[RGDfK(C)] for molecular imaging of tumor α(v)β(3) expression. *Bioconjug. Chem.* **2011**, *22*, 913–922. [CrossRef] [PubMed]
11. Huenges, E.; Parak, F.; Alexiou, C.; Jurgons, R.; Schmid, R.J.; Bergemann, C.; Henke, J.; Erhardt, W. Magnetic Drug Targeting–Biodistribution of the Magnetic Carrier and the Chemotherapeutic agent Mitoxantrone after Locoregional Cancer Treatment. *J. Drug Target.* **2003**, *11*, 139–149. [CrossRef] [PubMed]
12. Choi, J.; Park, J.C.; Nah, H.; Woo, S.; Oh, J.; Kim, K.M.; Cheon, G.J.; Chang, Y.; Yoo, J.; Cheon, J. A Hybrid Nanoparticle Probe for Dual-Modality Positron Emission Tomography and Magnetic Resonance Imaging. *Angew. Chem. Int. Ed.* **2008**, *47*, 6259–6262. [CrossRef] [PubMed]
13. Park, J.C.; Yu, M.K.; An, G.I.; Park, S.-I.; Oh, J.; Kim, H.J.; Kim, J.-H.; Wang, E.K.; Hong, I.-H.; Ha, Y.S.; et al. Facile Preparation of a Hybrid Nanoprobe for Triple-Modality Optical/PET/MR Imaging. *Small* **2010**, *6*, 2863–2868. [CrossRef] [PubMed]
14. Yang, C.; Zhu, R.; Wan, J.; Jiang, B.; Zhou, D.; Song, M.; Liu, F. Biological effects of irradiating hepatocellular carcinoma cells by internal exposure with 125I-labeled 5-iodo-2′-deoxyuridine-chitosan drug loading nanoparticles. *Cancer Biother. Radiopharm.* **2014**, *29*, 395–402. [CrossRef] [PubMed]
15. Chen, J.; Zhu, S.; Tong, L.; Li, J.; Chen, F.; Han, Y.; Zhao, M.; Xiong, W. Superparamagnetic iron oxide nanoparticles mediated $^{(131)}$I-hVEGF siRNA inhibits hepatocellular carcinoma tumor growth in nude mice. *BMC Cancer* **2014**, *14*, 114. [CrossRef] [PubMed]
16. Li, W.; Liu, Z.; Li, C.; Li, N.; Fang, L.; Chang, J.; Tan, J. Radionuclide therapy using ^{131}I-labeled anti-epidermal growth factor receptor-targeted nanoparticles suppresses cancer cell growth caused by EGFR overexpression. *J. Cancer Res. Clin. Oncol.* **2016**, *142*, 619–632. [CrossRef] [PubMed]
17. Sharma, R.; Xu, Y.; Kim, S.W.; Schueller, M.J.; Alexoff, D.; Smith, S.D.; Wang, W.; Schlyer, D. Carbon-11 radiolabeling of iron-oxide nanoparticles for dual-modality PET/MR imaging. *Nanoscale* **2013**, *5*, 7476. [CrossRef] [PubMed]
18. Chakravarty, R.; Goel, S.; Dash, A.; Cai, W. Radiolabeled inorganic nanoparticles for positron emission tomography imaging of cancer: An overview. *J. Nucl. Med. Mol. Imaging* **2017**, *67*, 181–204. [CrossRef]
19. Burke, B.P.; Cawthorne, C.; Archibald, S.J. Multimodal nanoparticle imaging agents: Design and applications. *Philos. Trans. A Math. Phys. Eng. Sci.* **2017**, *375*. [CrossRef] [PubMed]
20. Sun, X.; Cai, W.; Chen, X. Positron Emission Tomography Imaging Using Radiolabeled Inorganic Nanomaterials. *Acc. Chem. Res.* **2015**, *48*, 286–294. [CrossRef] [PubMed]
21. García-Toraño, E.; Peyrés Medina, V.; Romero, E.; Roteta, M. Measurement of the half-life of ^{68}Ga. *Appl. Radiat. Isot.* **2014**, *87*, 122–125. [CrossRef] [PubMed]
22. Martiniova, L.; De Palatis, L.; Etchebehere, E.; Ravizzini, G.; De Palatis, L.; Etchebehere, E.; Ravizzini, G. Gallium-68 in Medical Imaging. *Curr. Radiopharm.* **2016**, *9*, 187–207. [CrossRef] [PubMed]
23. Sweet, W.H.; Brownell, G.L. Localization of intracranial lesions by scanning with positron-emitting arsenic. *J. Am. Med. Assoc.* **1955**, *157*, 1183–1188. [CrossRef] [PubMed]
24. Gleason, G.I. A positron cow. *Int. J. Appl. Radiat. Isot.* **1960**, *8*, 90–94. [CrossRef]
25. Shealy, C.N.; Aronow, S.; Brownell, G.L. Gallium-68 As a Scanning Agent for Intracranial Lesions. *J. Nucl. Med.* **1964**, *5*, 161–167. [PubMed]
26. Greene, M.W.; Tucker, W.D. An improved gallium-68 cow. *Int. J. Appl. Radiat. Isot.* **1961**, *12*, 62–63. [CrossRef]
27. Yano, Y.; Anger, H. A Gallium68 Positron Cow for Medical Use. *J. Nucl. Med.* **1964**, 485–488.
28. Baum, R.P.; Rösch, F. (Eds.) *Theranostics, Gallium-68, and Other Radionuclides*; Recent Results in Cancer Research; Springer: Berlin/Heidelberg, Germany, 2013; Volume 194, ISBN 978-3-642-27993-5.
29. Rösch, F. Past, present and future of ^{68}Ge/^{68}Ga generators. *Appl. Radiat. Isot.* **2013**, *76*, 24–30. [CrossRef] [PubMed]
30. Zhernosekov, K.P.; Filosofov, D.V.; Baum, R.P.; Aschoff, P.; Bihl, H.; Razbash, A.A.; Jahn, M.; Jennewein, M.; Rosch, F. Processing of Generator-Produced ^{68}Ga for Medical Application. *J. Nucl. Med.* **2007**, *48*, 1741–1748. [CrossRef] [PubMed]

31. De Blois, E.; Sze Chan, H.; Naidoo, C.; Prince, D.; Krenning, E.P.; Breeman, W.A.P. Characteristics of SnO_2-based $^{68}Ge/^{68}Ga$ generator and aspects of radiolabelling DOTA-peptides. *Appl. Radiat. Isot.* **2011**, *69*, 308–315. [CrossRef] [PubMed]
32. Pellico, J.; Llop, J.; Fernández-Barahona, I.; Bhavesh, R.; Ruiz-Cabello, J.; Herranz, F. Iron Oxide Nanoradiomaterials: Combining Nanoscale Properties with Radioisotopes for Enhanced Molecular Imaging. *Contrast Media Mol. Imaging* **2017**, *2017*, 1–24. [CrossRef] [PubMed]
33. Chakravarty, R.; Chakraborty, S.; Ram, R.; Vatsa, R.; Bhusari, P.; Shukla, J.; Mittal, B.R.; Dash, A. Detailed evaluation of different $^{68}Ge/^{68}Ga$ generators: An attempt toward achieving efficient ^{68}Ga radiopharmacy. *J. Label. Compd. Radiopharm.* **2016**, *59*, 87–94. [CrossRef] [PubMed]
34. Velikyan, I. Prospective of ^{68}Ga-Radiopharmaceutical Development. *Theranostics* **2014**, *4*, 47–80. [CrossRef] [PubMed]
35. Banerjee, S.R.; Pomper, M.G. Clinical applications of Gallium-68. *Appl. Radiat. Isot.* **2013**, *76*, 2–13. [CrossRef] [PubMed]
36. Schlageter, N.L.; Carson, R.E.; Rapoport, S.I. Examination of blood-brain barrier permeability in dementia of the Alzheimer type with [^{68}Ga]EDTA and positron emission tomography. *J. Cereb. Blood Flow Metab.* **1987**, *7*, 1–8. [CrossRef] [PubMed]
37. Washburn, L.C.; Blair, L.D.; Byrd, B.L.; Sun, T.T. Comparison of ^{68}Ga-EDTA, [1-^{11}C]alpha-aminoisobutyric acid, and [^{99}mTc]sodium pertechnetate in an experimental blood-brain barrier lesion. *Int. J. Nucl. Med. Biol.* **1985**, *12*, 267–269. [CrossRef]
38. Nanni, C.; Errani, C.; Boriani, L.; Fantini, L.; Ambrosini, V.; Boschi, S.; Rubello, D.; Pettinato, C.; Mercuri, M.; Gasbarrini, A.; et al. ^{68}Ga-citrate PET/CT for evaluating patients with infections of the bone: Preliminary results. *J. Nucl. Med.* **2010**, *51*, 1932–1936. [CrossRef] [PubMed]
39. Kumar, V.; Boddeti, D.K.; Evans, S.G.; Angelides, S. $^{(68)}Ga$-Citrate-PET for diagnostic imaging of infection in rats and for intra-abdominal infection in a patient. *Curr. Radiopharm.* **2012**, *5*, 71–75. [CrossRef] [PubMed]
40. Fellner, M.; Biesalski, B.; Bausbacher, N.; Kubícek, V.; Hermann, P.; Rösch, F.; Thews, O. $^{(68)}Ga$-BPAMD: PET-imaging of bone metastases with a generator based positron emitter. *Nucl. Med. Biol.* **2012**, *39*, 993–999. [CrossRef] [PubMed]
41. Pfannkuchen, N.; Meckel, M.; Bergmann, R.; Bachmann, M.; Bal, C.; Sathekge, M.; Mohnike, W.; Baum, R.P.; Rösch, F. Novel Radiolabeled Bisphosphonates for PET Diagnosis and Endoradiotherapy of Bone Metastases. *Pharmaceuticals* **2017**, *10*, 45. [CrossRef] [PubMed]
42. Yang, B.Y.; Jeong, J.M.; Kim, Y.J.; Choi, J.Y.; Lee, Y.-S.; Lee, D.S.; Chung, J.-K.; Lee, M.C. Formulation of ^{68}Ga BAPEN kit for myocardial positron emission tomography imaging and biodistribution study. *Nucl. Med. Biol.* **2010**, *37*, 149–155. [CrossRef] [PubMed]
43. Tarkia, M.; Saraste, A.; Saanijoki, T.; Oikonen, V.; Vähäsilta, T.; Strandberg, M.; Stark, C.; Tolvanen, T.; Teräs, M.; Savunen, T.; et al. Evaluation of ^{68}Ga-labeled tracers for PET imaging of myocardial perfusion in pigs. *Nucl. Med. Biol.* **2012**, *39*, 715–723. [CrossRef] [PubMed]
44. Mueller, D.; Kulkarni, H.; Baum, R.P.; Odparlik, A. Rapid Synthesis of ^{68}Ga-labeled macroaggregated human serum albumin (MAA) for routine application in perfusion imaging using PET/CT. *Appl. Radiat. Isot.* **2017**, *122*, 72–77. [CrossRef] [PubMed]
45. Mathias, C.J.; Green, M.A. A convenient route to [^{68}Ga]Ga-MAA for use as a particulate PET perfusion tracer. *Appl. Radiat. Isot.* **2008**, *66*, 1910–1912. [CrossRef] [PubMed]
46. Even, G.A.; Green, M.A. Gallium-68-labeled macroaggregated human serum albumin, ^{68}Ga-MAA. *Int. J. Radic. Appl. Instrum. B* **1989**, *16*, 319–321. [CrossRef]
47. He, Q.; Xu, Z.; Zhang, B.; Hu, W.; Zhang, X. Tumor-Induced Osteomalacia Caused by a Parotid Basal Cell Adenoma Detected by ^{68}Ga-DOTANOC PET/CT. *Clin. Nucl. Med.* **2018**, *43*, e198–e199. [CrossRef] [PubMed]
48. Arunraj, S.T.; Parida, G.K.; Damle, N.A.; Arora, S.; Reddy, S.; Chakraborty, D.; Prabhu, M.; Tripathi, M.; Bal, C. ^{68}Ga-DOTANOC PET/CT in Medulloblastoma. *Clin. Nucl. Med.* **2018**, *43*, e145–e146. [CrossRef] [PubMed]
49. Malik, D.; Jois, A.; Singh, H.; Bora, G.S.; Basher, R.K.; Mittal, B.R. Metastatic Neuroblastoma in Adult Patient, Presenting as a Super Scan on ^{68}Ga-DOTANOC PET/CT Imaging. *Clin. Nucl. Med.* **2017**, *42*, 697–699. [CrossRef] [PubMed]

50. Ambrosini, V.; Castellucci, P.; Rubello, D.; Nanni, C.; Musto, A.; Allegri, V.; Montini, G.C.; Mattioli, S.; Grassetto, G.; Al-Nahhas, A.; et al. ^{68}Ga-DOTA-NOC: A new PET tracer for evaluating patients with bronchial carcinoid. *Nucl. Med. Commun.* **2009**, *30*, 281–286. [CrossRef] [PubMed]
51. Derlin, T.; Hartung, D.; Hueper, K. ^{68}Ga-DOTA-TATE PET/CT for Molecular Imaging of Somatostatin Receptor Expression in Extra-adrenal Paraganglioma in a Case of Complete Carney Triad. *Clin. Nucl. Med.* **2017**, *42*, e527–e528. [CrossRef] [PubMed]
52. Derlin, T.; Hueper, K.; Soudah, B. ^{68}Ga-DOTA-TATE PET/CT for Molecular Imaging of Somatostatin Receptor Expression in Metastasizing Epithelioid Hemangioendothelioma: Comparison with 18F-FDG. *Clin. Nucl. Med.* **2017**, *42*, e478–e479. [CrossRef] [PubMed]
53. Paquet, M.; Gauthé, M.; Zhang Yin, J.; Nataf, V.; Bélissant, O.; Orcel, P.; Roux, C.; Talbot, J.-N.; Montravers, F. Diagnostic performance and impact on patient management of ^{68}Ga-DOTA-TOC PET/CT for detecting osteomalacia-associated tumours. *Eur. J. Nucl. Med. Mol. Imaging* **2018**. [CrossRef] [PubMed]
54. Gauthé, M.; Sarfati, J.; Bourcigaux, N.; Christin-Maitre, S.; Talbot, J.-N.; Montravers, F. Pituitary Adenoma Recurrence Suspected on Central Hyperthyroidism Despite Empty Sella and Confirmed by ^{68}Ga-DOTA-TOC PET/CT. *Clin. Nucl. Med.* **2017**, *42*, 454–455. [CrossRef] [PubMed]
55. Morgat, C.; Vélayoudom-Céphise, F.-L.; Schwartz, P.; Guyot, M.; Gaye, D.; Vimont, D.; Schulz, J.; Mazère, J.; Nunes, M.-L.; Smith, D.; et al. Evaluation of $^{(68)}$Ga-DOTA-TOC PET/CT for the detection of duodenopancreatic neuroendocrine tumors in patients with MEN1. *Eur. J. Nucl. Med. Mol. Imaging* **2016**, *43*, 1258–1266. [CrossRef] [PubMed]
56. Liolios, C.; Buchmuller, B.; Bauder-Wüst, U.; Schäfer, M.; Leotta, K.; Haberkorn, U.; Eder, M.; Kopka, K. Monomeric and Dimeric ^{68}Ga-Labeled Bombesin Analogues for Positron Emission Tomography (PET) Imaging of Tumors Expressing Gastrin-Releasing Peptide Receptors (GRPrs). *J. Med. Chem.* **2018**, *61*, 2062–2074. [CrossRef] [PubMed]
57. Richter, S.; Wuest, M.; Bergman, C.N.; Krieger, S.; Rogers, B.E.; Wuest, F. Metabolically Stabilized $^{(68)}$Ga-NOTA-Bombesin for PET Imaging of Prostate Cancer and Influence of Protease Inhibitor Phosphoramidon. *Mol. Pharm.* **2016**, *13*, 1347–1357. [CrossRef] [PubMed]
58. Aljammaz, I.; Al-Otaibi, B.; Al-Hokbany, N.; Amer, S.; Okarvi, S. Development and pre-clinical evaluation of new ^{68}Ga-NOTA-folate conjugates for PET imaging of folate receptor-positive tumors. *Anticancer Res.* **2014**, *34*, 6547–6556. [PubMed]
59. Schwarzenböck, S.M.; Stenzel, J.; Otto, T.; Helldorff, H.V.; Bergner, C.; Kurth, J.; Polei, S.; Lindner, T.; Rauer, R.; Hohn, A.; et al. [^{68}Ga]pentixafor for CXCR4 imaging in a PC-3 prostate cancer xenograft model—Comparison with [18F]FDG PET/CT, MRI and ex vivo receptor expression. *Oncotarget* **2017**, *8*. [CrossRef] [PubMed]
60. Weiberg, D.; Thackeray, J.T.; Daum, G.; Sohns, J.M.; Kropf, S.; Wester, H.-J.; Ross, T.L.; Bengel, F.M.; Derlin, T. Clinical Molecular Imaging of Chemokine Receptor CXCR4 Expression in Atherosclerotic Plaque Using ^{68}Ga-Pentixafor PET: Correlation with Cardiovascular Risk Factors and Calcified Plaque Burden. *J. Nucl. Med.* **2018**, *59*, 266–272. [CrossRef] [PubMed]
61. Li, X.; Heber, D.; Leike, T.; Beitzke, D.; Lu, X.; Zhang, X.; Wei, Y.; Mitterhauser, M.; Wadsak, W.; Kropf, S.; et al. [^{68}Ga]Pentixafor-PET/MRI for the detection of Chemokine receptor 4 expression in atherosclerotic plaques. *Eur. J. Nucl. Med. Mol. Imaging* **2017**, 1–9. [CrossRef] [PubMed]
62. Werner, R.A.; Weich, A.; Higuchi, T.; Schmid, J.S.; Schirbel, A.; Lassmann, M.; Wild, V.; Rudelius, M.; Kudlich, T.; Herrmann, K.; et al. Imaging of Chemokine Receptor 4 Expression in Neuroendocrine Tumors—A Triple Tracer Comparative Approach. *Theranostics* **2017**, *7*, 1489–1498. [CrossRef] [PubMed]
63. Biener, J.; Wittstock, A.; Baumann, T.F.; Weissmüller, J.; Bäumer, M.; Hamza, A.V. Surface Chemistry in Nanoscale Materials. *Materials* **2009**, *2*, 2404–2428. [CrossRef]
64. Lamb, J.; Holland, J.P. Advanced Methods for Radiolabeling Multimodality Nanomedicines for SPECT/MRI and PET/MRI. *J. Nucl. Med.* **2018**, *59*, 382–389. [CrossRef] [PubMed]
65. Ma, M.T.; Cullinane, C.; Imberti, C.; Baguña Torres, J.; Terry, S.Y.A.; Roselt, P.; Hicks, R.J.; Blower, P.J. New Tris(hydroxypyridinone) Bifunctional Chelators Containing Isothiocyanate Groups Provide a Versatile Platform for Rapid One-Step Labeling and PET Imaging with $^{68}Ga^{3+}$. *Bioconjug. Chem.* **2016**, *27*, 309–318. [CrossRef] [PubMed]
66. Chakravarty, R.; Shukla, R.; Ram, R.; Tyagi, A.K.; Dash, A.; Venkatesh, M. Development of a nano-zirconia based ^{68}Ge/^{68}Ga generator for biomedical applications. *Nucl. Med. Biol.* **2011**, *38*, 575–583. [CrossRef] [PubMed]

67. Chen, F.; Ellison, P.A.; Lewis, C.M.; Hong, H.; Zhang, Y.; Shi, S.; Hernandez, R.; Meyerand, M.E.; Barnhart, T.E.; Cai, W. Chelator-Free Synthesis of a Dual-Modality PET/MRI Agent. *Angew. Chem. Int. Ed.* **2013**, *52*, 13319–13323. [CrossRef] [PubMed]
68. Long, N.V.; Teranishi, T.; Yang, Y.; Thi, C.M.; Cao, Y.; Nogami, M. Iron Oxide Nanoparticles for Next Generation Gas Sensors. *Int. J. Metall. Mater. Eng.* **2015**, *1*, 1–18. [CrossRef] [PubMed]
69. Evertsson, M.; Kjellman, P.; Cinthio, M.; Andersson, R.; Tran, T.A.; in't Zandt, R.; Grafström, G.; Toftevall, H.; Fredriksson, S.; Ingvar, C.; et al. Combined Magnetomotive ultrasound, PET/CT, and MR imaging of ^{68}Ga-labelled superparamagnetic iron oxide nanoparticles in rat sentinel lymph nodes in vivo. *Sci. Rep.* **2017**, *7*, 4824. [CrossRef] [PubMed]
70. Madru, R.; Tran, T.A.; Axelsson, J.; Ingvar, C.; Bibic, A.; Ståhlberg, F.; Knutsson, L.; Strand, S.-E. $^{(68)}$Ga-labeled superparamagnetic iron oxide nanoparticles (SPIONs) for multi-modality PET/MR/Cherenkov luminescence imaging of sentinel lymph nodes. *Am. J. Nucl. Med. Mol. Imaging* **2013**, *4*, 60–69. [PubMed]
71. Goel, S.; England, C.G.; Chen, F.; Cai, W. Positron emission tomography and nanotechnology: A dynamic duo for cancer theranostics. *Adv. Drug Deliv. Rev.* **2017**, *113*, 157–176. [CrossRef] [PubMed]
72. Pellico, J.; Ruiz-Cabello, J.; Saiz-Alía, M.; del Rosario, G.; Caja, S.; Montoya, M.; Fernández de Manuel, L.; Morales, M.P.; Gutiérrez, L.; Galiana, B.; et al. Fast synthesis and bioconjugation of ^{68}Ga core-doped extremely small iron oxide nanoparticles for PET/MR imaging. *Contrast Media Mol. Imaging* **2016**, *11*, 203–210. [CrossRef] [PubMed]
73. Pellico, J.; Lechuga-Vieco, A.V.; Almarza, E.; Hidalgo, A.; Mesa-Nuñez, C.; Fernández-Barahona, I.; Quintana, J.A.; Bueren, J.; Enríquez, J.A.; Ruiz-Cabello, J.; Herranz, F. In vivo imaging of lung inflammation with neutrophil-specific ^{68}Ga nano-radiotracer. *Sci. Rep.* **2017**, *7*, 13242. [CrossRef] [PubMed]
74. Kandanapitiye, M.S.; Gott, M.D.; Sharits, A.; Jurisson, S.S.; Woodward, P.M.; Huang, S.D. Incorporation of Gallium-68 into the crystal structure of Prussian blue to form $K_{68}Ga_xFe_{1-x}$ $[Fe(CN)_6]$ nanoparticles: Toward a novel bimodal PET/MRI imaging agent. *Dalt. Trans.* **2016**, *45*, 9174–9181. [CrossRef] [PubMed]
75. Smith, B.R.; Gambhir, S.S. Nanomaterials for In Vivo Imaging. *Chem. Rev.* **2017**, *117*, 901–986. [CrossRef] [PubMed]
76. Padmanabhan, P.; Kumar, A.; Kumar, S.; Chaudhary, R.K.; Gulyás, B. Nanoparticles in practice for molecular-imaging applications: An overview. *Acta Biomater.* **2016**, *41*, 1–16. [CrossRef] [PubMed]
77. Janib, S.M.; Moses, A.S.; MacKay, J.A. Imaging and drug delivery using theranostic nanoparticles. *Adv. Drug Deliv. Rev.* **2010**, *62*, 1052–1063. [CrossRef] [PubMed]
78. Bulte, J.W.; Modo, M.M.J. *Design and Applications of Nanoparticles in Biomedical Imaging*; Bulte, J.W.M., Modo, M.M.J., Eds.; Springer International Publishing: Cham, Switzerland, 2017; ISBN 978-3-319-42167-4.
79. Lee, H.; Gaddy, D.; Ventura, M.; Bernards, N.; de Souza, R.; Kirpotin, D.; Wickham, T.; Fitzgerald, J.; Zheng, J.; Hendriks, B.S. Companion Diagnostic 64 Cu-Liposome Positron Emission Tomography Enables Characterization of Drug Delivery to Tumors and Predicts Response to Cancer Nanomedicines. *Theranostics* **2018**, *8*, 2300–2312. [CrossRef] [PubMed]
80. Zheng, M.; Ruan, S.; Liu, S.; Sun, T.; Qu, D.; Zhao, H.; Xie, Z.; Gao, H.; Jing, X.; Sun, Z. Self-Targeting Fluorescent Carbon Dots for Diagnosis of Brain Cancer Cells. *ACS Nano* **2015**, *9*, 11455–11461. [CrossRef] [PubMed]
81. Zheng, B.; Von See, M.P.; Yu, E.; Gunel, B.; Lu, K.; Vazin, T.; Schaffer, D.V.; Goodwill, P.W.; Conolly, S.M. Quantitative magnetic particle imaging monitors the transplantation, biodistribution, and clearance of stem cells in vivo. *Theranostics* **2016**, *6*, 291–301. [CrossRef] [PubMed]
82. Marciello, M.; Pellico, J.; Fernandez-Barahona, I.; Herranz, F.; Ruiz-Cabello, J.; Filice, M. Recent advances in the preparation and application of multifunctional iron oxide and liposome-based nanosystems for multimodal diagnosis and therapy. *Interface Focus* **2016**, *6*, 20160055. [CrossRef] [PubMed]
83. Liu, X.; Zhong, Z.; Tang, Y.; Liang, B. Review on the synthesis and applications of Fe_3O_4 nanomaterials. *J. Nanomater.* **2013**, *2013*, 902538.
84. Lee, N.; Hyeon, T. Designed synthesis of uniformly sized iron oxide nanoparticles for efficient magnetic resonance imaging contrast agents. *Chem. Soc. Rev.* **2012**, *41*, 2575–2589. [CrossRef] [PubMed]
85. Pellico, J.; Lechuga-Vieco, A.V.; Benito, M.; García-Segura, J.M.; Fuster, V.; Ruiz-Cabello, J.; Herranz, F. Microwave-driven synthesis of bisphosphonate nanoparticles allows in vivo visualisation of atherosclerotic plaque. *RSC Adv.* **2015**, *5*, 1661–1665. [CrossRef]

86. Lechuga-Vieco, A.V.; Groult, H.; Pellico, J.; Mateo, J.; Enríquez, J.A.; Ruiz-Cabello, J.; Herranz, F. Protein corona and phospholipase activity drive selective accumulation of nanomicelles in atherosclerotic plaques. *Nanomed. Nanotechnol. Biol. Med.* **2018**, *14*, 643–650. [CrossRef] [PubMed]
87. Kim, B.H.; Lee, N.; Kim, H.; An, K.; Park, Y.I.; Choi, Y.; Shin, K.; Lee, Y.; Kwon, S.G.; Na, H.B.; et al. Large-Scale Synthesis of Uniform and Extremely Small-Sized Iron Oxide Nanoparticles for High-Resolution T 1 Magnetic Resonance Imaging Contrast Agents. *J. Am. Chem. Soc.* **2011**, *133*, 12624–12631. [CrossRef] [PubMed]
88. Hu, F.; Jia, Q.; Li, Y.; Gao, M. Facile synthesis of ultrasmall PEGylated iron oxide nanoparticles for dual-contrast T1- and T2-weighted magnetic resonance imaging. *Nanotechnology* **2011**, *22*, 245604. [CrossRef] [PubMed]
89. Pellico, J.; Ruiz-Cabello, J.; Fernández-Barahona, I.; Gutiérrez, L.; Lechuga-Vieco, A.V.; Enríquez, J.A.; Morales, M.P.; Herranz, F. One-Step Fast Synthesis of Nanoparticles for MRI: Coating Chemistry as the Key Variable Determining Positive or Negative Contrast. *Langmuir* **2017**, *33*, 10239–10247. [CrossRef] [PubMed]
90. Gleich, B.; Weizenecker, J. Tomographic imaging using the nonlinear response of magnetic particles. *Nature* **2005**, *435*, 1214–1217. [CrossRef] [PubMed]
91. Bulte, J.W.M.; Walczak, P.; Janowski, M.; Krishnan, K.M.; Arami, H.; Halkola, A.; Gleich, B.; Rahmer, J. Quantitative "Hot-Spot" Imaging of Transplanted Stem Cells Using Superparamagnetic Tracers and Magnetic Particle Imaging. *Tomography* **2015**, *1*, 91–97. [CrossRef] [PubMed]
92. Saritas, E.U.; Goodwill, P.W.; Croft, L.R.; Konkle, J.J.; Lu, K.; Zheng, B.; Conolly, S.M. Magnetic particle imaging (MPI) for NMR and MRI researchers. *J. Magn. Reson.* **2013**, *229*, 116–126. [CrossRef] [PubMed]
93. Zheng, B.; Vazin, T.; Goodwill, P.W.; Conway, A.; Verma, A.; Ulku Saritas, E.; Schaffer, D.; Conolly, S.M. Magnetic particle imaging tracks the long-term fate of in vivo neural cell implants with high image contrast. *Sci. Rep.* **2015**, *5*, 14055. [CrossRef] [PubMed]
94. Ferguson, R.M.; Khandhar, A.P.; Kemp, S.J.; Arami, H.; Saritas, E.U.; Croft, L.R.; Konkle, J.; Goodwill, P.W.; Halkola, A.; Rahmer, J.; et al. Magnetic particle imaging with tailored iron oxide nanoparticle tracers. *IEEE Trans. Med. Imaging* **2015**, *34*, 1077–1084. [CrossRef] [PubMed]
95. Lee, H.-Y.; Li, Z.; Chen, K.; Hsu, A.R.; Xu, C.; Xie, J.; Sun, S.; Chen, X. PET/MRI Dual-Modality Tumor Imaging Using Arginine-Glycine-Aspartic (RGD)-Conjugated Radiolabeled Iron Oxide Nanoparticles. *J. Nucl. Med.* **2008**, *49*, 1371–1379. [CrossRef] [PubMed]
96. Kim, S.; Chae, M.K.; Yim, M.S.; Jeong, I.H.; Cho, J.; Lee, C.; Ryu, E.K. Hybrid PET/MR imaging of tumors using an oleanolic acid-conjugated nanoparticle. *Biomaterials* **2013**, *34*, 8114–8121. [CrossRef] [PubMed]
97. Moon, S.-H.; Yang, B.Y.; Kim, Y.J.; Hong, M.K.; Lee, Y.-S.; Lee, D.S.; Chung, J.-K.; Jeong, J.M. Development of a complementary PET/MR dual-modal imaging probe for targeting prostate-specific membrane antigen (PSMA). *Nanomed. Nanotechnol. Biol. Med.* **2016**, *12*, 871–879. [CrossRef] [PubMed]
98. Franchini, M.C.; Pucci, A.; Locatelli, E.; Naddaka, M.; Milani, F.; Passoni, L.; Matteoli, M.; Llop, J.; Reese, T.; Israel, L.L.; et al. Biocompatible nanocomposite for PET/MRI hybrid imaging. *Int. J. Nanomed.* **2012**, *7*, 6021–6033. [CrossRef] [PubMed]
99. Yang, B.Y.; Moon, S.-H.; Seelam, S.R.; Jeon, M.J.; Lee, Y.-S.; Lee, D.S.; Chung, J.-K.; Kim, Y.I.; Jeong, J.M. Development of a multimodal imaging probe by encapsulating iron oxide nanoparticles with functionalized amphiphiles for lymph node imaging. *Nanomedicine* **2015**, *10*, 1899–1910. [CrossRef] [PubMed]
100. Thorek, D.L.J.; Ulmert, D.; Diop, N.-F.M.; Lupu, M.E.; Doran, M.G.; Huang, R.; Abou, D.S.; Larson, S.M.; Grimm, J. Non-invasive mapping of deep-tissue lymph nodes in live animals using a multimodal PET/MRI nanoparticle. *Nat. Commun.* **2014**, *5*, 2166–2171. [CrossRef] [PubMed]
101. Lahooti, A.; Sarkar, S.; Saligheh Rad, H.; Gholami, A.; Nosrati, S.; Muller, R.N.; Laurent, S.; Grüttner, C.; Geramifar, P.; Yousefnia, H.; et al. PEGylated superparamagnetic iron oxide nanoparticles labeled with ^{68}Ga as a PET/MRI contrast agent: A biodistribution study. *J. Radioanal. Nucl. Chem.* **2017**, *311*, 769–774. [CrossRef]
102. Soo Choi, H.; Liu, W.; Misra, P.; Tanaka, E.; Zimmer, J.P.; Itty Ipe, B.; Bawendi, M.G.; Frangioni, J.V. Renal clearance of quantum dots. *Nat. Biotechnol.* **2007**, *25*, 1165–1170. [CrossRef] [PubMed]
103. Briley-Saebo, K.; Bjrnerud, A.; Grant, D.; Ahlstrom, H.; Berg, T.; Kindberg, G.M. Hepatic cellular distribution and degradation of iron oxide nanoparticles following single intravenous injection in rats: Implications for magnetic resonance imaging. *Cell Tissue Res.* **2004**, *316*, 315–323. [CrossRef] [PubMed]

104. Song, G.; Petschauer, J.; Madden, A.; Zamboni, W. Nanoparticles and the Mononuclear Phagocyte System: Pharmacokinetics and Applications for Inflammatory Diseases. *Curr. Rheumatol. Rev.* **2014**, *10*, 22–34. [CrossRef] [PubMed]
105. Karageorgou, M.; Vranješ-Djurić, S.; Radović, M.; Lyberopoulou, A.; Antić, B.; Rouchota, M.; Gazouli, M.; Loudos, G.; Xanthopoulos, S.; Sideratou, Z.; et al. Gallium-68 Labeled Iron Oxide Nanoparticles Coated with 2,3-Dicarboxypropane-1,1-diphosphonic Acid as a Potential PET/MR Imaging Agent: A Proof-of-Concept Study. *Contrast Media Mol. Imaging* **2017**, *2017*, 1–13. [CrossRef] [PubMed]
106. Burke, B.P.; Baghdadi, N.; Kownacka, A.E.; Nigam, S.; Clemente, G.S.; Al-Yassiry, M.M.; Domarkas, J.; Lorch, M.; Pickles, M.; Gibbs, P.; et al. Chelator free gallium-68 radiolabelling of silica coated iron oxide nanorods via surface interactions. *Nanoscale* **2015**, *7*, 14889–14896. [CrossRef] [PubMed]
107. Bouziotis, P.; Stellas, D.; Thomas, E.; Truillet, C.; Tsoukalas, C.; Lux, F.; Tsotakos, T.; Xanthopoulos, S.; Paravatou-Petsotas, M.; Gaitanis, A.; et al. ^{68}Ga-radiolabeled AGuIX nanoparticles as dual-modality imaging agents for PET/MRI-guided radiation therapy. *Nanomedicine* **2017**, *12*, 1561–1574. [CrossRef] [PubMed]
108. Ghai, A.; Singh, B.; Panwar Hazari, P.; Schultz, M.K.; Parmar, A.; Kumar, P.; Sharma, S.; Dhawan, D.; Kumar Mishra, A. Radiolabeling optimization and characterization of ^{68}Ga labeled DOTA–polyamido-amine dendrimer conjugate—Animal biodistribution and PET imaging results. *Appl. Radiat. Isot.* **2015**, *105*, 40–46. [CrossRef] [PubMed]
109. Prabhakar, U.; Maeda, H.; Jain, R.K.; Sevick-Muraca, E.M.; Zamboni, W.; Farokhzad, O.C.; Barry, S.T.; Gabizon, A.; Grodzinski, P.; Blakey, D.C. Challenges and key considerations of the enhanced permeability and retention effect for nanomedicine drug delivery in oncology. *Cancer Res.* **2013**, *73*, 2412–2417. [CrossRef] [PubMed]
110. Huynh, E.; Zheng, G. Cancer nanomedicine: Addressing the dark side of the enhanced permeability and retention effect. *Nanomedicine* **2015**, *10*, 1993–1995. [CrossRef] [PubMed]
111. Pattni, B.S.; Chupin, V.V.; Torchilin, V.P. New Developments in Liposomal Drug Delivery. *Chem. Rev.* **2015**, *115*, 10938–10966. [CrossRef] [PubMed]
112. Nogueira, E.; Gomes, A.C.; Preto, A.; Cavaco-Paulo, A. Design of liposomal formulations for cell targeting. *Colloids Surf. B Biointerfaces* **2015**, *136*, 514–526. [CrossRef] [PubMed]
113. Mura, S.; Nicolas, J.; Couvreur, P. Stimuli-responsive nanocarriers for drug delivery. *Nat. Mater.* **2013**, *12*, 991–1003. [CrossRef] [PubMed]
114. Eloy, J.O.; Claro de Souza, M.; Petrilli, R.; Barcellos, J.P.A.; Lee, R.J.; Marchetti, J.M. Liposomes as carriers of hydrophilic small molecule drugs: Strategies to enhance encapsulation and delivery. *Colloids Surf. B Biointerfaces* **2014**, *123*, 345–363. [CrossRef] [PubMed]
115. Ren, L.; Chen, S.; Li, H.; Zhang, Z.; Zhong, J.; Liu, M.; Zhou, X. MRI-guided liposomes for targeted tandem chemotherapy and therapeutic response prediction. *Acta Biomater.* **2016**, *35*, 260–268. [CrossRef] [PubMed]
116. Rizzitelli, S.; Giustetto, P.; Faletto, D.; Delli Castelli, D.; Aime, S.; Terreno, E. The release of Doxorubicin from liposomes monitored by MRI and triggered by a combination of US stimuli led to a complete tumor regression in a breast cancer mouse model. *J. Control. Release* **2016**, *230*, 57–63. [CrossRef] [PubMed]
117. Guo, H.; Chen, W.; Sun, X.; Liu, Y.N.; Li, J.; Wang, J. Theranostic magnetoliposomes coated by carboxymethyl dextran with controlled release by low-frequency alternating magnetic field. *Carbohydr. Polym.* **2015**, *118*, 209–217. [CrossRef] [PubMed]
118. Blocker, S.J.; Douglas, K.A.; Polin, L.A.; Lee, H.; Hendriks, B.S.; Lalo, E.; Chen, W.; Shields, A.F. Liposomal 64Cu-PET Imaging of Anti-VEGF Drug Effects on Liposomal Delivery to Colon Cancer Xenografts. *Theranostics* **2017**, *7*, 4229–4239. [CrossRef] [PubMed]
119. Malinge, J.; Géraudie, B.; Savel, P.; Nataf, V.; Prignon, A.; Provost, C.; Zhang, Y.; Ou, P.; Kerrou, K.; Talbot, J.-N.; et al. Liposomes for PET and MR Imaging and for Dual Targeting (Magnetic Field/Glucose Moiety): Synthesis, Properties, and in Vivo Studies. *Mol. Pharm.* **2017**, *14*, 406–414. [CrossRef] [PubMed]
120. Jensen, A.I.; Severin, G.W.; Hansen, A.E.; Fliedner, F.P.; Eliasen, R.; Parhamifar, L.; Kjær, A.; Andresen, T.L.; Henriksen, J.R. Remote-loading of liposomes with manganese-52 and in vivo evaluation of the stabilities of 52 Mn-DOTA and 64 Cu-DOTA using radiolabelled liposomes and PET imaging. *J. Control. Release* **2018**, *269*, 100–109. [CrossRef] [PubMed]
121. Beziere, N.; Lozano, N.; Nunes, A.; Salichs, J.; Queiros, D.; Kostarelos, K.; Ntziachristos, V. Dynamic imaging of PEGylated indocyanine green (ICG) liposomes within the tumor microenvironment using multi-spectral optoacoustic tomography (MSOT). *Biomaterials* **2015**, *37*, 415–424. [CrossRef] [PubMed]

122. Helbok, A.; Decristoforo, C.; Dobrozemsky, G.; Rangger, C.; Diederen, E.; Stark, B.; Prassl, R.; von Guggenberg, E. Radiolabeling of lipid-based nanoparticles for diagnostics and therapeutic applications: A comparison using different radiometals. *J. Liposome Res.* **2010**, *20*, 219–227. [CrossRef] [PubMed]
123. Lee, J.H.; Park, G.; Hong, G.H.; Choi, J.; Choi, H.S. Design considerations for targeted optical contrast agents. *Quant. Imaging Med. Surg.* **2012**, *2*, 266–273. [CrossRef] [PubMed]
124. Bhatia, D.; Arumugam, S.; Nasilowski, M.; Joshi, H.; Wunder, C.; Chambon, V.; Prakash, V.; Grazon, C.; Nadal, B.; Maiti, P.K.; et al. Quantum dot-loaded monofunctionalized DNA icosahedra for single-particle tracking of endocytic pathways. *Nat. Nanotechnol.* **2016**, *11*, 1112–1119. [CrossRef] [PubMed]
125. Wichner, S.M.; Mann, V.R.; Powers, A.S.; Segal, M.A.; Mir, M.; Bandaria, J.N.; DeWitt, M.A.; Darzacq, X.; Yildiz, A.; Cohen, B.E. Covalent Protein Labeling and Improved Single-Molecule Optical Properties of Aqueous CdSe/CdS Quantum Dots. *ACS Nano* **2017**. [CrossRef] [PubMed]
126. Wegner, K.D.; Hildebrandt, N. Quantum dots: Bright and versatile in vitro and in vivo fluorescence imaging biosensors. *Chem. Soc. Rev.* **2015**, *44*, 4792–4834. [CrossRef] [PubMed]
127. Yu, W.W.; Wang, Y.A.; Peng, X. Formation and Stability of Size-, Shape-, and Structure-Controlled CdTe Nanocrystals: Ligand Effects on Monomers and Nanocrystals. *Chem. Mater.* **2003**, *15*, 4300–4308. [CrossRef]
128. Bailey, R.E.; Nie, S. Alloyed Semiconductor Quantum Dots: Tuning the Optical Properties without Changing the Particle Size. *J. Am. Chem. Soc.* **2003**, *125*, 7100–7106. [CrossRef] [PubMed]
129. Gao, X.; Cui, Y.; Levenson, R.M.; Chung, L.W.K.; Nie, S. In vivo cancer targeting and imaging with semiconductor quantum dots. *Nat. Biotechnol.* **2004**, *22*, 969–976. [CrossRef] [PubMed]
130. Wu, X.; Liu, H.; Liu, J.; Haley, K.N.; Treadway, J.A.; Larson, J.P.; Ge, N.; Peale, F.; Bruchez, M.P. Immunofluorescent labeling of cancer marker Her2 and other cellular targets with semiconductor quantum dots. *Nat. Biotechnol.* **2003**, *21*, 41–46. [CrossRef] [PubMed]
131. Sun, X.; Huang, X.; Guo, J.; Zhu, W.; Ding, Y.; Niu, G.; Wang, A.; Kiesewetter, D.O.; Wang, Z.L.; Sun, S.; et al. Self-illuminating 64Cu-Doped CdSe/ZnS nanocrystals for in vivo tumor imaging. *J. Am. Chem. Soc.* **2014**, *136*, 1706–1709. [CrossRef] [PubMed]
132. Li, D.; Jing, P.; Sun, L.; An, Y.; Shan, X.; Lu, X.; Zhou, D.; Han, D.; Shen, D.; Zhai, Y.; et al. Near-Infrared Excitation/Emission and Multiphoton-Induced Fluorescence of Carbon Dots. *Adv. Mater.* **2018**, *30*, 1705913. [CrossRef] [PubMed]
133. Yang, W.; Zhang, H.; Lai, J.; Peng, X.; Hu, Y.; Gu, W.; Ye, L. Carbon dots with red-shifted photoluminescence by fluorine doping for optical bio-imaging. *Carbon N. Y.* **2018**, *128*, 78–85. [CrossRef]
134. Huang, Y.-F.; Zhou, X.; Zhou, R.; Zhang, H.; Kang, K.-B.; Zhao, M.; Peng, Y.; Wang, Q.; Zhang, H.-L.; Qiu, W.-Y. One-Pot Synthesis of Highly Luminescent Carbon Quantum Dots and Their Nontoxic Ingestion by Zebrafish for In Vivo Imaging. *Chem. A Eur. J.* **2014**, *20*, 5640–5648. [CrossRef] [PubMed]
135. Fazaeli, Y.; Zare, H.; Karimi, S.; Rahighi, R.; Feizi, S. Novel aspects of application of cadmium telluride quantum dots nanostructures in radiation oncology. *Appl. Phys. A* **2017**, *123*, 507. [CrossRef]
136. Zhou, J.; Liu, Z.; Li, F. Upconversion nanophosphors for small-animal imaging. *Chem. Soc. Rev.* **2012**, *41*, 1323–1349. [CrossRef] [PubMed]
137. Wang, C.; Cheng, L.; Xu, H.; Liu, Z. Towards whole-body imaging at the single cell level using ultra-sensitive stem cell labeling with oligo-arginine modified upconversion nanoparticles. *Biomaterials* **2012**, *33*, 4872–4881. [CrossRef] [PubMed]
138. Auzel, F. Upconversion and Anti-Stokes Processes with f and d Ions in Solids. *Chem. Rev.* **2003**. [CrossRef]
139. Groult, H.; Ruiz-Cabello, J.; Pellico, J.; Lechuga-Vieco, A.V.; Bhavesh, R.; Zamai, M.; Almarza, E.; Martín-Padura, I.; Cantelar, E.; Martínez-Alcázar, M.P.; et al. Parallel Multifunctionalization of Nanoparticles: A One-Step Modular Approach for in Vivo Imaging. *Bioconjug. Chem.* **2015**, *26*, 153–160. [CrossRef] [PubMed]
140. Park, Y.I.; Lee, K.T.; Suh, Y.D.; Hyeon, T. Upconverting nanoparticles: A versatile platform for wide-field two-photon microscopy and multi-modal in vivo imaging. *Chem. Soc. Rev.* **2015**, *44*, 1302–1317. [CrossRef] [PubMed]
141. Maji, S.K.; Sreejith, S.; Joseph, J.; Lin, M.; He, T.; Tong, Y.; Sun, H.; Yu, S.W.-K.; Zhao, Y. Upconversion Nanoparticles as a Contrast Agent for Photoacoustic Imaging in Live Mice. *Adv. Mater.* **2014**, *26*, 5633–5638. [CrossRef] [PubMed]
142. Kumar, R.; Nyk, M.; Ohulchanskyy, T.Y.; Flask, C.A.; Prasad, P.N. Combined optical and MR bloimaging using rare earth ion doped NaYF4nanocrystals. *Adv. Funct. Mater.* **2009**, *19*, 853–859. [CrossRef]

143. Park, Y.I.; Kim, H.M.; Kim, J.H.; Moon, K.C.; Yoo, B.; Lee, K.T.; Lee, N.; Choi, Y.; Park, W.; Ling, D.; et al. Theranostic probe based on lanthanide-doped nanoparticles for simultaneous in vivo dual-modal imaging and photodynamic therapy. *Adv. Mater.* **2012**, *24*, 5755–5761. [CrossRef] [PubMed]
144. Zhou, J.; Yu, M.; Sun, Y.; Zhang, X.; Zhu, X.; Wu, Z.; Wu, D.; Li, F. Fluorine-18-labeled $Gd^{3+}/Yb^{3+}/Er^{3+}$ co-doped $NaYF_4$ nanophosphors for multimodality PET/MR/UCL imaging. *Biomaterials* **2011**, *32*, 1148–1156. [CrossRef] [PubMed]
145. Liu, Y.; Ai, K.; Liu, J.; Yuan, Q.; He, Y.; Lu, L. A high-performance ytterbium-based nanoparticulate contrast agent for in vivo X-ray computed tomography imaging. *Angew. Chem. Int. Ed.* **2012**, *51*, 1437–1442. [CrossRef] [PubMed]
146. Zhu, X.; Zhou, J.; Chen, M.; Shi, M.; Feng, W.; Li, F. Core-shell Fe_3O_4@$NaLuF_4$: Yb,Er/Tm nanostructure for MRI, CT and upconversion luminescence tri-modality imaging. *Biomaterials* **2012**, *33*, 4618–4627. [CrossRef] [PubMed]
147. Liu, Q.; Sun, Y.; Li, C.; Zhou, J.; Li, C.; Yang, T.; Zhang, X.; Yi, T.; Wu, D.; Li, F. 18F-labeled magnetic-upconversion nanophosphors via rare-earth cation-assisted ligand assembly. *ACS Nano* **2011**, *5*, 3146–3157. [CrossRef] [PubMed]
148. Gallo, J.; Alam, I.S.; Jin, J.; Gu, Y.-J.; Aboagye, E.O.; Wong, W.-T.; Long, N.J. PET imaging with multimodal upconversion nanoparticles. *Dalt. Trans.* **2014**, *43*, 5535. [CrossRef] [PubMed]
149. Song, J.; Yang, X.; Yang, Z.; Lin, L.; Liu, Y.; Zhou, Z.; Shen, Z.; Yu, G.; Dai, Y.; Jacobson, O.; et al. Rational Design of Branched Nanoporous Gold Nanoshells with Enhanced Physico-Optical Properties for Optical Imaging and Cancer Therapy. *ACS Nano* **2017**, *11*, 6102–6113. [CrossRef] [PubMed]
150. Hainfeld, J.F.; Slatkin, D.N.; Focella, T.M.; Smilowitz, H.M. Gold nanoparticles: A new X-ray contrast agent. *Br. J. Radiol.* **2006**, *79*, 248–253. [CrossRef] [PubMed]
151. Huang, Y.; Coman, D.; Hyder, F.; Ali, M.M. Dendrimer-Based Responsive MRI Contrast Agents (G1-G4) for Biosensor Imaging of Redundant Deviation in Shifts (BIRDS). *Bioconjug. Chem.* **2015**, *26*, 2315–2323. [CrossRef] [PubMed]
152. Mendoza-Nava, H.; Ferro-Flores, G.; Ramírez, F.M.; Ocampo-García, B.; Santos-Cuevas, C.; Azorín-Vega, E.; Jiménez-Mancilla, N.; Luna-Gutiérrez, M.; Isaac-Olivé, K. Fluorescent, Plasmonic, and Radiotherapeutic Properties of the ^{177}Lu–Dendrimer-AuNP–Folate–Bombesin Nanoprobe Located Inside Cancer Cells. *Mol. Imaging* **2017**, *16*, 153601211770476. [CrossRef] [PubMed]
153. Xie, L.; Wang, G.; Zhou, H.; Zhang, F.; Guo, Z.; Liu, C.; Zhang, X.; Zhu, L. Functional long circulating single walled carbon nanotubes for fluorescent/photoacoustic imaging-guided enhanced phototherapy. *Biomaterials* **2016**, *103*, 219–228. [CrossRef] [PubMed]
154. Budhathoki-Uprety, J.; Langenbacher, R.E.; Jena, P.V.; Roxbury, D.; Heller, D.A. A Carbon Nanotube Optical Sensor Reports Nuclear Entry via a Noncanonical Pathway. *ACS Nano* **2017**, *11*, 3875–3882. [CrossRef] [PubMed]
155. Di Paola, M.; Quarta, A.; Conversano, F.; Sbenaglia, E.A.; Bettini, S.; Valli, L.; Gigli, G.; Casciaro, S. Human Hepatocarcinoma Cell Targeting by Glypican-3 Ligand Peptide Functionalized Silica Nanoparticles: Implications for Ultrasound Molecular Imaging. *Langmuir* **2017**, *33*, 4490–4499. [CrossRef] [PubMed]
156. Rainone, P.; Riva, B.; Belloli, S.; Sudati, F.; Ripamonti, M.; Verderio, P.; Colombo, M.; Colzani, B.; Gilardi, M.C.; Moresco, R.M.; et al. Development of 99mTc-radiolabeled nanosilica for targeted detection of HER2-positive breast cancer. *Int. J. Nanomed.* **2017**, *12*, 3447–3461. [CrossRef] [PubMed]
157. Frigell, J.; García, I.; Gómez-Vallejo, V.; Llop, J.; Penadés, S. ^{68}Ga-Labeled Gold Glyconanoparticles for Exploring Blood–Brain Barrier Permeability: Preparation, Biodistribution Studies, and Improved Brain Uptake via Neuropeptide Conjugation. *J. Am. Chem. Soc.* **2014**, *136*, 449–457. [CrossRef] [PubMed]
158. Truillet, C.; Bouziotis, P.; Tsoukalas, C.; Brugière, J.; Martini, M.; Sancey, L.; Brichart, T.; Denat, F.; Boschetti, F.; Darbost, U.; et al. Ultrasmall particles for Gd-MRI and ^{68}Ga-PET dual imaging. *Contrast Media Mol. Imaging* **2015**, *10*, 309–319. [CrossRef] [PubMed]
159. Polyak, A.; Naszalyi Nagy, L.; Mihaly, J.; Görres, S.; Wittneben, A.; Leiter, I.; Bankstahl, J.P.; Sajti, L.; Kellermayer, M.; Zrínyi, M.; et al. Preparation and ^{68}Ga-radiolabeling of porous zirconia nanoparticle platform for PET/CT-imaging guided drug delivery. *J. Pharm. Biomed. Anal.* **2017**, *137*, 146–150. [CrossRef] [PubMed]

160. Shaffer, T.M.; Wall, M.A.; Harmsen, S.; Longo, V.A.; Drain, C.M.; Kircher, M.F.; Grimm, J. Silica Nanoparticles as Substrates for Chelator-free Labeling of Oxophilic Radioisotopes. *Nano Lett.* **2015**, *15*, 864–868. [CrossRef] [PubMed]
161. Cartier, R.; Kaufner, L.; Paulke, B.R.; Wüstneck, R.; Pietschmann, S.; Michel, R.; Bruhn, H.; Pison, U. Latex nanoparticles for multimodal imaging and detection in vivo. *Nanotechnology* **2007**, *18*, 195102. [CrossRef]